Energy Landscape Analysis with Automated Region-of-Interest Selection via Genetic Algorithms

Koichiro Mori
Graduate School of Life and Medical Sciences, Doshisha University, Kyoto, Japan

Tomoyuki Hiroyasu
Department of Biomedical Sciences and Informatics, Doshisha University, Kyoto, Japan

Satoru Hiwa (corresponding author)
Department of Biomedical Sciences and Informatics, Doshisha University, Kyoto, Japan
E-mail: shiwa@mail.doshisha.ac.jp
Postal address: 1-3 Tatara Miyakodani, Kyotanabe, Kyoto 610-0394, Japan

Abstract

Understanding brain dynamics is essential for advancing cognitive and clinical neuroscience. Energy landscape analysis (ELA), based on the pairwise maximum entropy model, is a powerful framework to characterize brain activity as transitions among discrete states defined by regional activity patterns. However, traditional approaches require a predefined set of regions of interest (ROIs), usually chosen based on prior knowledge from hypothesis-driven studies, which introduces subjectivity and may overlook previously unknown patterns. To overcome this limitation, we developed a new ELA framework enhanced by automated ROI selection using genetic algorithm optimization, called ELA/GAopt. ELA/GAopt employs a genetic algorithm to select ROI subsets that maximize model fitting accuracy while accounting for individual variability. We applied ELA/GAopt to two independent resting-state functional magnetic resonance imaging datasets. In Scenario 1, we tested how well the method generalizes using the Creativity dataset (OpenNeuro: ds002330), which includes 66 healthy adults (29 males, 36 females, and one non-binary individual; average age 26.6 ± 4.3 years). ELA/GAopt was performed on a discovery set ($n = 31$), and the optimized ROI sets were validated on a test set ($n = 30$). Over 100 independent optimization runs, the selected ROI sets achieved significantly higher objective function values than randomly chosen ROI sets (permutation test, $p < 0.05$, false discovery-rate corrected). The similarity of local minimum states between discovery and test sets was also significantly higher for ELA/GAopt than for random selection ($p < 0.05$). These results confirm the reproducibility and generalizability of the proposed approach. In

Scenarios 2–4, we analyzed data from 293 participants in the Autism Brain Imaging Data Exchange II dataset, including 157 with autism spectrum disorder (ASD) and 136 typically developing controls (CTL) from discovery cohort A and validated findings in an independent cohort (54 ASD and 72 CTL participants). ELA/GAopt showed that ASD participants tend to visit local minima characterized by global co-activation of selected ROIs, especially within sensory-motor and visual networks. Additionally, ROI sets optimized for one group (ASD or CTL) did not generalize across groups, with significant differences in the number and structure of local minima (Mann–Whitney U test, $p < 0.05$, false discovery-rate corrected). These findings demonstrate that ELA/GAopt offers a robust, data-driven approach to modeling brain state dynamics, minimizing biases from predefined ROI selection. It improves reproducibility and could aid in discovering neuroimaging biomarkers for clinical conditions.

Keywords

Functional MRI, Autism spectrum disorder, Brain dynamics, Energy landscape analysis, Genetic algorithm

Introduction

Interpreting system behavior from multidimensional observation data is essential in various scientific fields, including neuroscience. Energy landscape analysis (ELA) is one such method that applies the Ising model to multidimensional data, introducing the concept of energy to each pattern and visualizing the stability and transitions of emerging patterns as an energy landscape. The Ising model, also known as the pairwise maximum entropy model (pMEM),[1,2] was initially introduced in statistical physics to explain the properties of magnetic materials. It is highly versatile and facilitates the interpretation of system dynamics as interactions between paired elements. The energy landscape derived from observed multidimensional data enables a bird's-eye view of the system's dynamics. A notable application in neuroscience was introduced by Watanabe et al.,[3] who applied the ELA to functional MRI (fMRI) data, establishing a data-driven approach to extract brain dynamics from neuroimaging data. Subsequently, Ezaki et al.[4] investigated fundamental issues of ELA for neuroimaging data and developed the Energy Landscape Analysis Toolbox (ELAT). Their contributions have made ELA applicable to diverse neuroimaging datasets, including various neurological conditions and disorders,[1,5,6] and significantly advanced understanding in the neuroscience field.[1,3–5,7–14]

Despite its success, the current ELA paradigm faces several challenges due to its analytical constraints, including the length of data and the selection of the region of interest (ROI). The ELA requires sufficient data length to ensure the accurate fitting of the pMEM, which necessitates an exponential increase in the required data length with the number of variables, roughly doubling for each additional variable. Masuda et al.[15] estimated that the practical upper limit for the number of ROIs (i.e., data dimension) that can be included in ELA without compromising accuracy is around 10 to 15, depending on the available data length.[15]

In contrast, whole-brain parcellation typically yields hundreds of regions, depending on the atlas used (e.g., 116 for the AAL,[16] 264 for the Power atlas,[17] and 100 to 1000 for the Schaefer 2018 atlas[18,19]). Therefore, analysts are required to narrow down the candidate ROIs substantially. Common approaches include selecting regions implicated in relevant cognitive processes based on prior studies or choosing representative regions from well-known functional networks. However, these approaches inherently reflect existing knowledge, introducing selection bias and reducing the data-driven nature of ELA. Thus, while ELA is conceptually a data-driven method,[4,15] the practical constraints of the data length and ROI selection often render it partially hypothesis-driven—an issue that

undermines the objectivity and exploratory potential of the analysis.

To overcome this limitation, we propose a genetic algorithm-based optimization framework for automatically selecting ROI subsets that ensure sufficient pMEM fitting accuracy while preserving the data-driven nature of ELA. Genetic algorithms (GAs) are a class of heuristic optimization techniques inspired by natural selection and evolution. They are widely used to obtain approximate solutions for nonlinear optimization problems, including neuroimaging applications.[20–23] In our proposed approach, the pre-selection of ROIs is formulated as a combinatorial optimization problem. The objective function incorporates both the pMEM fitting accuracy and the inter-individual variability of the model parameters, and the optimal subset is selected from the complete set of whole brain regions. This procedure eliminates the need for manually selecting ROIs based on expert judgment or prior knowledge, thereby enabling a fully data-driven implementation of ELA—an advancement that has not been previously achieved in this field. Here, we refer to this automated method as ELA/GAopt and evaluate its effectiveness using large-scale, open-access fMRI datasets, demonstrating its applicability across both cognitive and translational neuroscience domains.

Specifically, to validate the effectiveness of our approach, we apply it to two large-scale open neuroimaging datasets. First, we assess its generalizability by testing whether the brain state dynamics identified using the proposed method are reproducible on the dataset of healthy participants. Then, we investigate its applicability to clinical neuroscience by analyzing resting-state fMRI data from individuals with autism spectrum disorder (ASD) and typically developing controls (CTL). This analysis enables us to investigate whether the method can identify condition-specific patterns in brain state transitions. These applications demonstrate the potential of our approach to enhance the objectivity and reliability of brain dynamics modeling, thereby contributing to data-driven knowledge discovery in cognitive and translational neuroscience.

Materials and methods

Overview of ELA/GAopt: Energy landscape analysis with automated ROI selection via genetic algorithms

The proposed ELA/GAopt framework aims to automate the selection of ROIs in ELA through a combinatorial optimization approach. It involves iteratively selecting ROI subsets, performing ELA, particularly fitting the pMEM, and evaluating the results until specified conditions are met.

To solve this combinatorial optimization problem, we employ a GA. GAs are heuristic optimization techniques characterized by multipoint exploration enabling the generation of multiple candidate solutions (i.e., ROI subsets) in parallel. Each solution is evaluated using a fitness function that quantifies the goodness of the solution, which is based on the ELA output in this case. This strategy helps avoid local optima and improves the robustness of the search process.

A schematic overview of ELA/GAopt in neuroimaging data is presented in Figure 1. The following sections describe each component of the framework and detailed analysis procedures.

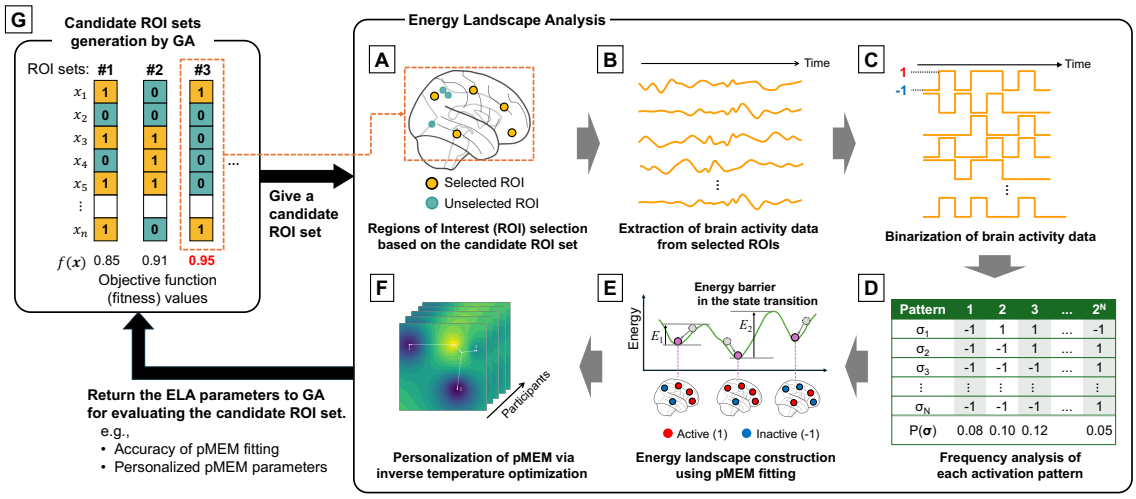

Figure 1 Schematic overview of ELA/GAopt framework.

Framework of ELA

Binarization of multidimensional time series data

The input to ELA is an *N*-dimensional discrete time series obtained from *N* ROIs:

$$\{\boldsymbol{x}(1), \dots, \boldsymbol{x}(t_{\max})\}$$

where $\boldsymbol{x}(t) \in \mathbb{R}^N$ for $t \in \{1, \dots, t_{\max}\}$ is the ROI signal vector at time t, and $t_{\max}$ is the total number of time points (i.e., the length of the observed time series), Each vector $\boldsymbol{x}(t)$ is defined as:

$$\boldsymbol{x}(t) = \left(x_1(t), \dots, x_N(t)\right)$$

In ELA, multidimensional signals at each time point are converted into binary patterns. Each ROI signal $x_i(t)$ is binarized using a threshold θ_i, where $i \in \{1, \dots, N\}$. The binarized value $\sigma_i(t) \in \{-1, +1\}$ is defined as:

$$\sigma_i(t) = \begin{cases} +1 & \text{if } x_i(t) > \theta_i \\ -1 & \text{otherwise} \end{cases}$$

The full binarized vector at each time point *t* is:

$$\boldsymbol{\sigma}(t) = \left(\sigma_1(t), \dots, \sigma_N(t)\right)$$

Each $\sigma_i(t)$ represents the binary activation state of the i-th ROI at time t, where $+1$ indicates "active" and -1 indicates "inactive". Thus, the signal pattern at time t is given by the N-dimensional binary vector $\boldsymbol{\sigma}(t)$, also referred to as an activity pattern or active pattern. For notational simplicity, the time index t may be omitted where appropriate. In total, there are 2^N possible activity patterns, representing all binary combinations of ROI states.

Fitting a pMEM

A pMEM is fitted to binarized time series data to estimate the energy associated with each observed signal pattern. For neuroimaging data, this allows modeling the distribution and dynamics of brain states based on observed frequencies of binary activation patterns. First, we compute the empirical distribution $P_{\text{empirical}}(\boldsymbol{\sigma})$ which represents the relative frequency of each activity pattern observed in the data (Figure 1D). Let $\boldsymbol{\sigma}^{(1)}, \dots, \boldsymbol{\sigma}^{(2^N)}$ denote all possible binary activity patterns. Then, $P_{\text{empirical}}(\boldsymbol{\sigma})$ is simply the proportion of time points where pattern $\boldsymbol{\sigma}$ occurs, calculated by:

$$\sum_{k=1}^{2^N} P_{\text{empirical}}\left(\boldsymbol{\sigma}^{(k)}\right) = 1$$

That is, the empirical frequency distribution $P_{\text{empirical}}(\boldsymbol{\sigma})$ is calculated by counting how many times each of the 2^N possible binary patterns appear in the binarized time series and dividing by the total number of time points. The empirical mean signal pattern of the i-th ROI is:

$$\langle \sigma_i \rangle_{\text{empirical}} = \frac{1}{t_{\max}} \sum_{t=1}^{t_{\max}} \sigma_i(t)$$

The empirical pairwise correlation between the i-th and j-th ROIs is:

$$\langle \sigma_i \sigma_j \rangle_{\text{empirical}} = \frac{1}{t_{\max}} \sum_{t=1}^{t_{\max}} \sigma_i(t)\sigma_j(t)$$

The pMEM estimates a probability distribution $P(\boldsymbol{\sigma})$ that matches these first- and second-order moments while maximizing entropy. The result is the Boltzmann distribution:

$$P(\boldsymbol{\sigma}) = \frac{e^{-E(\boldsymbol{\sigma})}}{\sum_{k=1}^{2^N} e^{-E(\boldsymbol{\sigma}^{(k)})}}$$

Equivalently, the distribution can be expressed in terms of model parameters $\boldsymbol{h}$ and $\boldsymbol{J}$ as:

$$P(\boldsymbol{\sigma}|\boldsymbol{h},\boldsymbol{J}) = \frac{e^{-E(\boldsymbol{\sigma}|\boldsymbol{h},\boldsymbol{J})}}{\sum_{\{\boldsymbol{\sigma}'\}} e^{-E(\boldsymbol{\sigma}'|\boldsymbol{h},\boldsymbol{J})}}$$

with the energy function:

$$E(\boldsymbol{\sigma}|\boldsymbol{h},\boldsymbol{J}) = -\sum_{i=1}^{N} h_i\sigma_i - \frac{1}{2}\sum_{i=1}^{N}\sum_{i=1,j\neq 1}^{N} J_{ij}\sigma_i\,\sigma_{ij}$$

This formulation models the energy of each pattern based on ROI-wise signal tendencies (h_i) and pairwise interactions among ROIs (J_{ij}).

In this study, the model parameters $\boldsymbol{h}$ and $\boldsymbol{J}$ were estimated by pseudo-likelihood maximization, following the implementation described by Ezaki et al.[4] Full details of the fitting procedure, including gradient ascent optimization, are available in their original publication. Specifically, we used a Python implementation of the ELA toolbox developed by Oku (https://github.com/okumakito/elapy).[24]

Accuracy metrics for pMEM fitting

To evaluate the quality of the fitted pMEM, we used the Shannon entropy-based and the Kullback-Leibler (KL) divergence-based metrics. In this study, the arithmetic mean of these two metrics was used. Definitions of the accuracy metrics are described in Appendix 1 of the Supplementary materials.

Personalization of pMEM via temperature optimization

In standard ELA, individual data is concatenated into a group-level dataset to estimate a single set of $\boldsymbol{h}$ and $\boldsymbol{J}$ parameters representing group characteristics. Although it is theoretically possible to fit pMEM to individual data, this approach is rarely adopted in practice because it requires a large amount of data to achieve stable estimation. For example, in typical fMRI datasets, the number of time points per individual is often insufficient to reliably estimate all parameters of the model. Therefore, pMEM is typically estimated using concatenated group-level data for robustness and accuracy. However, when individual variability needs consideration, personalization of the pMEM becomes essential. Ruffini et al.[25] proposed a two-step pMEM parameter optimization method in which the inverse temperature parameter β, which characterizes the Boltzmann distribution, is optimized for each individual data while keeping the group-derived $\boldsymbol{h}$ and $\boldsymbol{J}$ parameters fixed. This approach allows group-level trends to be captured by $\boldsymbol{h}$ and $\boldsymbol{J}$, while individual differences are represented by β. The detailed procedure is described in Appendix 2 of the Supplementary materials.

Energy landscape and local minimum

By fitting a pMEM to the observed time series, the energy associated with any given pattern $\boldsymbol{\sigma}$ can be estimated. Since each pattern $\boldsymbol{\sigma}$ lies in a high-dimensional binary space defined over N ROIs, its neighboring patterns are those that differ from $\boldsymbol{\sigma}$ by exactly one bit (i.e., Hamming distance = 1). For example, consider $\boldsymbol{\sigma} = (1, 1, -1, 1)$ with $N = 4$. This pattern has four neighbors obtained by flipping each element. These N neighbors form vertices of an N-dimensional hypercube surrounding $\boldsymbol{\sigma}$. This structure allows us to interpret the temporal dynamics as transitions among vertices within this energy-defined space (that is, energy landscape).

Under the Boltzmann distribution, states with lower energy tend to appear more frequently, making local minima in the energy landscape particularly important. In ELA, such local minima are interpreted as representative signal patterns (states). The dynamics between these stable patterns, that is, how the system transitions from one to another, provide insights into the system structure. Moreover, the characteristics of the constructed energy landscape can be visualized using a contour plot, which highlights the energy barriers between local minima, as shown in Figure 1E.

Automated ROI selection using a genetic algorithm

We introduce a mechanism to automatically determine the optimal subset of ROIs within the aforementioned ELA framework. In this study, we formulate ROI selection as a combinatorial optimization problem. The goal is to select a subset of ROIs that maximizes the quality of the pMEM fitting while capturing individual variability.

A critical aspect of combinatorial optimization is defining the objective function, which quantifies how well a candidate solution satisfies the desired properties. In this work, we define the objective function as the sum of:

- The fitting accuracy of the pMEM is represented by the similarity between the model and empirical distributions.
- The variance of the personalized inverse temperature parameter (β) across all participants, derived from the individualized Boltzmann distribution.

Let $\boldsymbol{x} \in \{0,1\}^d$ be a binary vector encoding the selection of d ROIs available, where $x_k = 1$ if the k-th ROI is selected and zero otherwise, and $N \leq d$ is the total number of ROIs to select. Then, the optimization problem is formulated as:

$$\text{Maximize } f(\boldsymbol{x}) = r(\boldsymbol{x}) + \frac{1}{n}\sum_{k=1}^{m}(\beta_k(\boldsymbol{x}) - \bar{\beta})^2$$

$$\text{subject to} \sum_{k=1}^{d} x_k = N$$

Here, $r(\boldsymbol{x})$ denotes a pMEM fitting accuracy when ROIs specified by $\boldsymbol{x}$ are used, and $\beta_k(\boldsymbol{x})$ is the optimized inverse temperature for the k-th participant using the selected ROI subset $\boldsymbol{x}$. The mean value of $\beta_k(\boldsymbol{x})$ for m participants is denoted by $\bar{\beta}$. The constraint ensures that exactly N ROIs are selected from the d available candidates.

This objective function can be flexibly determined based on the analysis goals. For example, if the analyst expects the pMEM model parameters to correlate with data features, such correlations can be included as an additional term in the objective function. The above definition of the objective function is a general example that can be used for various purposes. By optimizing this function with a GA, the proposed framework enables data-driven selection of ROI subsets.

For the implementation of a GA, we used a standard evolutionary framework based on Holland's original design,[26] using the Deap library.[27] We employed tournament selection, two-point crossover, and bit-flip mutation. To ensure the feasibility of the solutions, we incorporated a repair strategy called Lamarckian repair,[28] which iteratively modifies infeasible solutions until they satisfy the specified constraints. Specifically, if the number of selected ROIs exceeds the prescribed limit, a subset of ROIs with a value of 1 (i.e., indicating selection) is randomly chosen and flipped to 0. The GA iteratively explored the optimal combinations of the ROIs for ELA. The full implementation details and parameter settings are provided in Supplementary Algorithm 1 and Supplementary Table 1.

Datasets

To evaluate the performance and generalizability of the proposed ELA/GAopt framework, we applied it to two independent resting-state fMRI datasets. In the following sections, we overview the datasets used, including their preprocessing methods, as well as the analysis scenarios that utilize these datasets.

Creativity Dataset

We employed a publicly available dataset related to creativity, hosted on OpenNeuro (dataset ID: ds002330).[29] A total of 66 healthy adults completed a neuroimaging session and four creativity assessments: the Abbreviated Torrance Test for Adults (ATTA) in verbal and visual formats, the Creative Behavior Inventory (CBI), and the Creative Achievement Questionnaire (CAQ). One participant did not complete the ATTA due to logistical reasons. The sample consisted of 29 males, 36 females, and one non-binary individual, with a mean age of 26.6 years (SD = 4.3).

MRI data included T1- and T2-weighted structural images, resting-state fMR images, and diffusion-weighted images (DWIs). After excluding participants with missing ATTA scores or insufficient data quality, the final analytic sample included 61 participants. These were stratified into a discovery set ($n = 31$) and a test set ($n = 30$) based on their ATTA verbal scores. The descriptive characteristics of two subsets are provided in Supplementary Table 2.

ABIDE II Dataset

We used data from the Autism Brain Imaging Data Exchange II (ABIDE II), which provides a large multi-site resting-state fMRI and anatomical dataset for investigating ASD. Data from 17 sites were included after excluding two sites due to preprocessing incompatibility. The original dataset included 1,114 participants (ASD: 521, CTL: 593); 81 participants were removed due to preprocessing issues, resulting in a final sample of 1,033 participants.

Each remaining participant provided at least one resting-state fMRI scan and a high-resolution T1-weighted structural image. Basic demographic and cognitive data (e.g., age, sex, IQ) were available for all individuals. Detailed acquisition protocols and site-specific procedures are described in the related publications.[30,31]

To balance site-specific variance, we grouped the dataset into three cohorts of approximately 300 participants each (A, C, and D) and an additional cohort (B) of around 100 participants used for independent validation. The distribution of participants across sites and cohorts is provided in Supplementary Table 3.

Data preprocessing

Details of image preprocessing of two independent datasets are described in Appendix 3 of the Supplementary Materials.[32–34] Additionally, we used different atlases for each dataset: the Dosenbach atlas for Creativity Dataset ($d = 160$),[35–39] and the Power 264 atlas for ABIDE II Dataset ($d = 264$),[17] respectively. The BOLD time courses were extracted from the spherical mask with a 4 mm radius centered at each ROI coordinate, then averaged within the ROI. The average time courses were considered representative of brain activity in each ROI. Finally, the ROI-averaged activity data was then binarized using the threshold of the time-averaged value of each activity for the ELA input.

Statistical analysis

Scenario 1: Validation of generalizability of ELA/GAopt using the Creativity dataset

The objective of Scenario 1 was to evaluate whether the proposed automated ROI

selection method avoids overfitting and selection bias. We first applied ELA/GAopt to the discovery dataset in 100 independent runs, each with a different initial GA population, resulting in 100 optimized ROI sets. Following Ezaki et al (2017)[4], who demonstrated that the accuracy of pMEM fitting scales with $l/2^N$ (i.e., the average number of visits per activity pattern), the number of ROIs in Scenario 1 was fixed at 10 ($N = 10$). They reported that each activity pattern should be visited approximately 5 and 16 times on average to achieve accuracies of 0.8 and 0.9, respectively. For the $l = 9170$ data points in this scenario, choosing $N = 10$ ($2^{10} = 1024$) yields $l/2^N \approx 9.0$ visits per pattern, which lies between 5 and 16; thus, we expect an accuracy between 0.8 and 0.9.

With the resulting ROIs chosen by ELA/GAopt for 100 trials, a one-tailed binomial test was performed to assess whether each brain region was selected more frequently than expected by chance. False discovery rate (FDR) correction was performed for multiple comparisons. To quantify the effect size for these binomial comparisons, Cohen's h was calculated. This process ensured the detection of consistently selected ROIs for multiple GA optimization runs.

Next, each of the 100 optimized ROI sets was applied to the test dataset using standard ELA. In parallel, we generated 100 randomly selected ROI sets, each also consisting of 10 ROIs, and applied them to both the discovery and test datasets using the same ELA procedure. In total, this yielded two groups of ROI sets, optimized, and randomly selected, for comparative analysis.

We tested two hypotheses: 1) the optimized ROI sets provide better objective function values (i.e., the sum of pMEM fitting accuracy and inter-individual variance of the inverse temperature) than random sets, and this advantage generalizes to the test data, and 2) the local minimum patterns identified in the discovery dataset are reproducible in the test dataset.

For Hypothesis 1, we compared the objective function values of the optimized and random ROI sets on the test dataset using permutation testing. Specifically, the objective values from both sets were pooled and the group labels (optimized vs. random) were shuffled 10,000 times to generate a null distribution. For each permutation, the mean objective value for each group was computed. A p-value was then derived by comparing the actual difference in mean objective values between the optimized and random groups to this null distribution. Statistical significance was assessed at $p < 0.05$. In addition, effect size (Cohen's d) was calculated to quantify the observed differences between optimized and random ROI sets.

For Hypothesis 2, we quantified the similarity of local minimum patterns between the discovery and test datasets. Each pattern among the 2^N possible signal patterns (for N ROIs) were assigned a unique ID. For each ELA run, we generated an ID vector indicating the presence (1) or absence (0) of each pattern as a local minimum in the estimated energy landscape. We then calculated the Hamming distance between ID vectors from the discovery and test datasets for each ROI set. A smaller Hamming distance indicates greater reproducibility of the local minimum patterns. The Hamming distances of the optimized and random ROI sets were compared using a permutation test (with 10,000 permutations), with significance assessed at $p < 0.05$. In addition, Cohen's d was computed to quantify the effect size of the difference in the Hamming distance. All permutation tests were one-tailed.

Scenario 2: Group-level comparison of brain dynamics on the ABIDE II Dataset

Scenario 2 investigated whether the different brain dynamics of two separate groups were observed on the single energy landscape constructed using ELA/GAopt on the concatenated dataset. Specifically, we aimed to observe group-specific brain dynamics on the energy landscape estimated on the mixed dataset of ASD and CTL groups, in a fully data-driven manner using ELA/GAopt. To confirm this, we extract the local minimum patterns more frequently visited in each group.

A total of 293 participants (ASD group: 157 and CTL group: 136, from Cohort A) were used as the discovery set. An independent dataset of 126 participants (ASD: 54, CTL: 72, Cohort B) was used for validation. The number of selected ROIs for the ABIDE II dataset in Scenarios 2 was fixed at 13, following the same procedure as in Scenario 1. The ELA/GAopt was performed 100 times for each of the 293 participants. Then, we evaluated how frequently each ROI was selected across trials. To determine whether specific ROIs were selected more frequently than expected by chance, a binomial test was performed for each ROI. The test assessed whether the observed selection frequency exceeded the expected frequency under a null hypothesis of random selection. The resulting p-values were corrected for multiple comparisons using FDR correction, and statistically significant ROIs (FDR-adjusted $p < 0.05,$ one-tailed) were identified. To quantify the magnitude of deviation from chance-level selection, Cohen's h was calculated as the effect size. These ROIs were considered consistently important across trials and served as the basis for further group comparisons.

To perform group-level comparisons of local minimum patterns, we selected representative ELA/GAopt trials in which all selected ROIs were among those identified as

statistically significant in the above binomial tests. These representative trials then estimated energy landscapes, and the probability of visiting each local minimum was computed for all individuals.

To compare these probabilities between the ASD and CTL groups, we applied the Mann-Whitney U test for each identified local minimum (FDR-adjusted $p < 0.05$, two-tailed). To quantify group difference magnitude, we also calculated the effect size (r) based on the Z-statistic from the Mann-Whitney U test. To evaluate the robustness of observed group-level differences, the same analysis was repeated on an independent validation dataset (Cohort B), following the same ROI configuration and statistical testing procedures.

Scenarios 3 and 4: Estimation of ASD- or CTL-optimized energy landscapes on the ABIDE II Dataset

In Scenario 3, we investigated whether a set of ROIs optimized for the ASD group could yield distinctive brain state characteristics. To this end, ELA/GAopt was executed 100 times for the ASD group (131 participants, Cohort C) to identify ROIs optimized for this group. The number of selected ROIs was fixed at 12, following the same procedure as in Scenario 1. As in Scenario 2, we assessed the selection frequency of each ROI across trials and identified consistently selected ROIs using a binomial test (FDR-adjusted $p < 0.05$, one-tailed). For these binomial tests, Cohen's h was calculated as the effect size.

The resulting ASD-optimized ROI set was then applied to an independent CTL dataset (175 participants from Cohort C) to evaluate whether the same ROI configuration would produce distinct energy landscape characteristics. Specifically, the number of local minima identified in the CTL group was compared to that in the ASD group using the Mann-Whitney U test. To quantify the magnitude of group differences, we also calculated the effect size (r) based on the Z-statistic from the Mann-Whitney U test (two-tailed). We hypothesized that if the ASD-optimized ROIs reflect ASD-specific brain state dynamics, applying them to CTL data would result in significantly different energy landscape structures—particularly in the number or configuration of local minima—between the two groups.

Scenario 4 mirrored this procedure for the CTL group. ELA/GAopt was conducted 100 times for CTL participants (168 individuals, Cohort D), and the resulting CTL-optimized ROI set was applied to an independent ASD dataset (140 participants, Cohort D). ROI selection analysis and statistical testing were conducted in the same manner as in Scenario 3. We hypothesized that if the CTL-optimized ROIs captured control-specific dynamics, applying them to ASD data would similarly yield distinct energy landscape structures.

Computational environment

We used a computing workstation equipped with an Intel Core (TM) i9-14900K CPU, a 7.7 GHz 24-core processor, and an NVIDIA GeForce RTX 4080 16GB GPU for ELA/GAopt execution.

Result

Scenario 1

Supplementary Figure 1 shows the convergence of the objective function with ELA/GAopt over 1000 generations for 100 runs with different starting populations. As the optimization problem was formulated as a maximization task, the objective function value increased with each generation. All runs converged to a range between 1.00 and 1.10.

Based on the 100 ELA/GAopt runs, a binomial test was conducted to assess whether each ROI was selected more frequently than expected by chance. Eighteen ROIs were statistically significant after FDR correction ($p < 0.05$), as listed in Figure 2 and Supplementary Table 4, which also includes the anatomical coordinates and associated functional networks for each ROI. Additionally, the distribution of selected ROIs across the 100 runs is presented in Supplementary Figure 2, which shows the total number of times each ROI was selected.

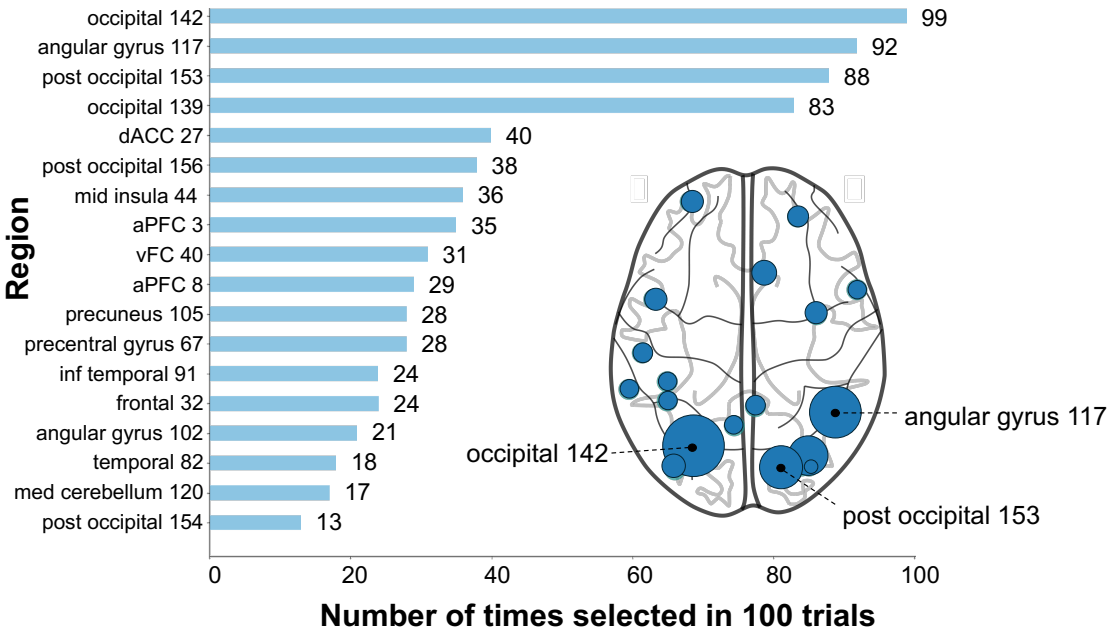

Figure 2 Selection frequency of each ROI across 100 runs of ELA/GAopt (Scenario 1).

To test the reproducibility of the local minimum patterns across datasets, we calculated the Hamming distance between ID vectors of the discovery and test datasets. Figure 3A and D show that the Hamming distances were significantly smaller for the optimized ROIs compared to the randomly selected ROIs (permutation test, 10,000 permutations, $p = 0.0025$, FDR-corrected, Cohen's d: 0.408), indicating greater pattern stability with the optimized ROIs.

Finally, Figure 3B, C, E, and F summarize the comparison of the objective function values in both the discovery and test sets. Permutation testing revealed that the values for the optimized ROI sets were significantly higher than those of the randomly selected sets in the discovery set ($p < 0.001$, FDR-corrected, Cohen's d: 5.63). Crucially, this significant advantage also generalized to the independent test set ($p < 0.001$, FDR-corrected, Cohen's d:2.51), confirming the generalizability and effectiveness of the proposed ROI selection framework.

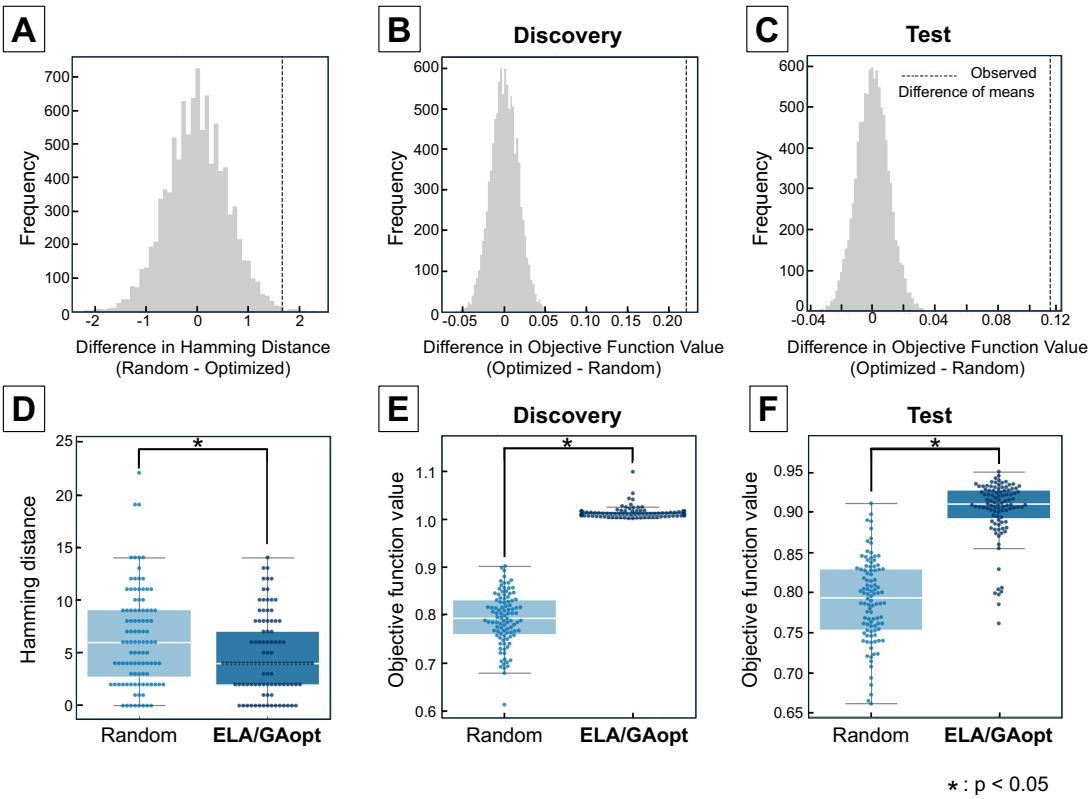

Figure 3 Reproducibility of local minimum patterns across discovery and test datasets.

Scenario 2

Supplementary Figure 4 illustrates the convergence of the objective function over 1000 generations during ELA/GAopt, conducted in 100 independent runs with different initial populations. As with Scenario 1, the optimization process consistently improved the objective function value, with most runs converging by the end of the generation window.

Based on the ROI selection results from the 100 runs, we performed a statistical analysis using a binomial test to determine whether each brain region was selected more frequently than expected by chance. The resulting p-values were adjusted using the FDR correction to account for multiple comparisons. Brain regions identified as significant are presented in Figure 4 and Supplementary Table 5.

Additionally, the overall distribution of ROI selections across the 100 trials is presented in Supplementary Figure 5. The selection frequency indicates how often ROIs from each functional network were selected during the automated ROI selection process in ELA/GAopt.

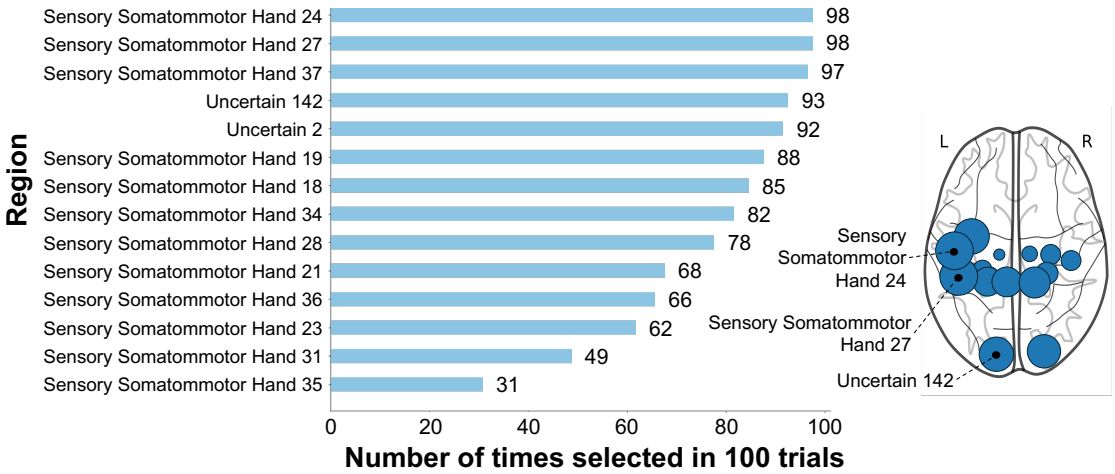

Figure 4 Selection frequency of each ROI across 100 runs of ELA/GAopt (Scenario 2).

To compare the probability of visiting each local minimum between the ASD and CTL groups, a representative trial was selected from the 100 ELA/GAopt runs. Since the objective function values were sufficiently high across all trials, they were not suitable as selection criteria. Instead, we focused on two trials where all selected ROIs were identified as being significantly more frequently selected than expected by chance, based on the binomial test with FDR correction ($p < 0.05$).

In the first representative trial, 13 ROIs were selected (Figure 5A), and 12 distinct local minimum states were identified in Cohort A (Figure 5A, left panel). To assess group differences in the probability of visiting each of the four most prominent local minima (as listed in Table 1), Mann-Whitney U tests were conducted, followed by FDR correction. Significant between-group differences were observed (FDR-corrected $p < 0.05$).

To validate the robustness of these findings, the same analysis was repeated on the independent validation dataset (Cohort B). In this cohort, six distinct local minimum states were observed Figure 5A, right panel), and notably, the local minimum state common to both cohorts (shared the same state number). These validation results supported the conclusion that the ASD group exhibited a higher probability of visiting a local minimum characterized by the simultaneous activation of all selected ROIs.

A second representative trial was similarly identified based on ROI selection consistency (Figure 5B). In this trial, 13 ROIs were selected, and 10 unique local minimum states were observed in Cohort A (Figure 5B, left panel). Mann-Whitney U tests revealed significant differences in the occurrence probability for seven states between groups ($p < 0.05$, FDR corrected; see Table 2). Again, several states were more frequently visited by the ASD group, while others were predominant in the CTL group.

Validation on Cohort B confirmed the presence of seven local minima (Figure 5B, right panel), with overlapping state numbers across cohorts. Group differences in visiting specific states (notably States 2) were replicated, further supporting the generalizability of the observed ASD-specific dynamics.

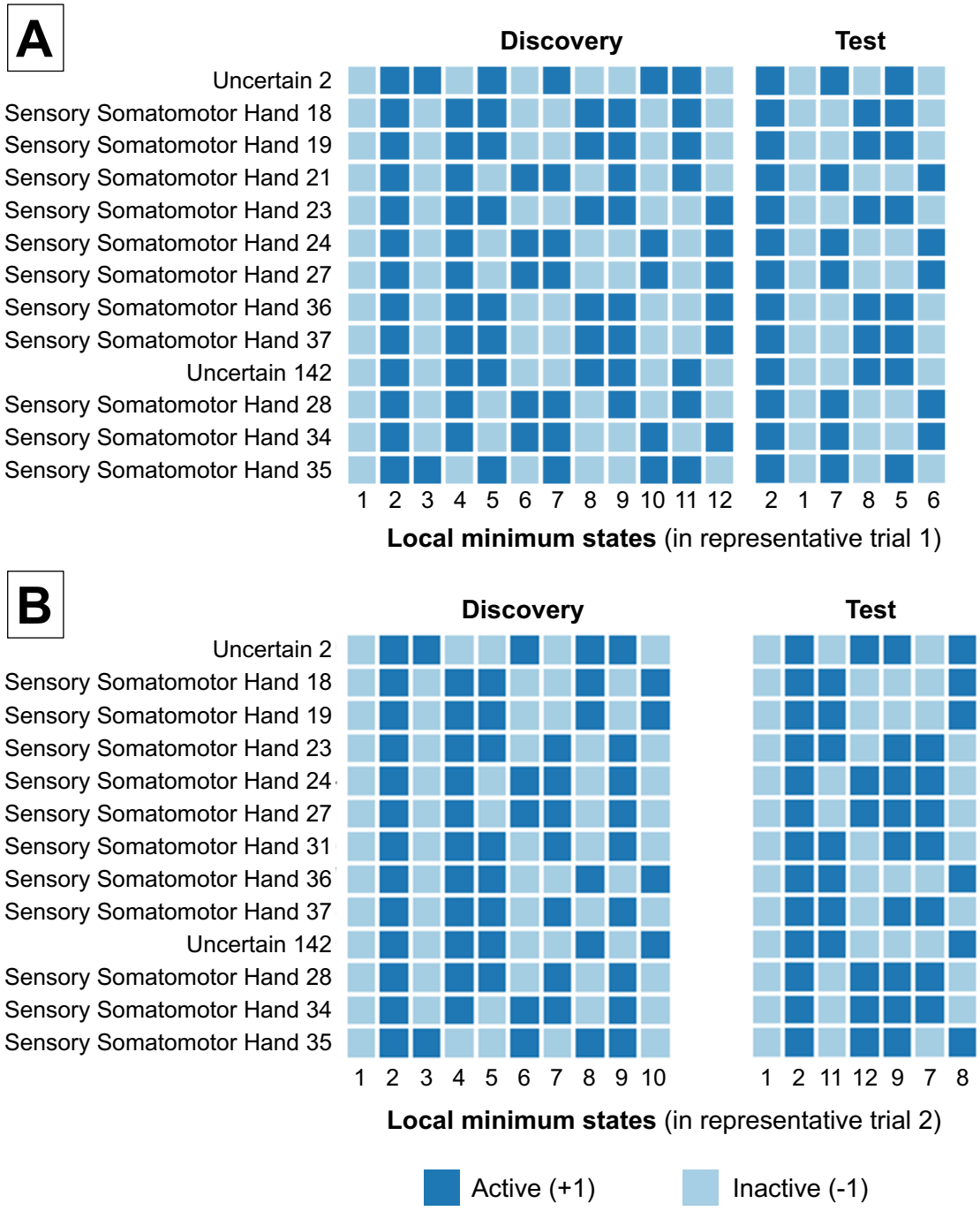

Figure 5. Observed local minimum states for representative trials 1 (A) and 2 (B).

Table 1. Frequency of local minimum occurrence in representative trial 1 (Significant results in bold; FDR-corrected p-value).

		probability of appearance			
State number	Cohort	ASD	CTL	*p*-value (FDR corrected)	Effect size *r*

1	A	0.367	0.361	0.436	0.0531
1	B	0.464	0.466	**0.00386**	-0.276
2	A	0.349	0.344	**0.00897**	0.179
2	B	0.463	0.461	**0.00386**	0.285
3	A	0.106	0.111	0.0536	-0.129
4	A	0.104	0.107	0.0888	-0.114
5	A	0.0175	0.0176	0.432	-0.0577
5	B	0.0156	0.0152	0.767	-0.0266
6	A	0.0168	0.0174	0.498	-0.0435
6	B	0.00662	0.00734	**2.41E-10**	-0.588
7	A	0.00784	0.00846	**0.00941**	-0.173
7	B	0.0297	0.0293	0.742	-0.0446
8	A	0.00797	0.00820	0.0526	-0.134
8	B	0.0210	0.0207	0.143	0.149
9	A	0.00665	0.00741	**0.00897**	-0.194
10	A	0.00751	0.00801	**0.00897**	-0.179
11	A	0.00562	0.00552	0.290	0.0760
12	A	0.00444	0.00460	0.699	-0.0226

Table 2 Frequency of local minimum occurrence in representative trial 2 (Significant results in bold; FDR-corrected p-values)

		probability of appearance			
State number	Cohort	ASD	CTL	*p*-value (FDR corrected)	Effect size *r*
1	A	0.369	0.365	0.540	0.0359
1	B	0.472	0.475	**3.09E-05**	-0.396
2	A	0.355	0.351	**0.00740**	0.174
2	B	0.461	0.456	**2.08E-08**	0.529
3	A	0.0948	0.0984	**0.0380**	-0.130
4	A	0.0950	0.0981	0.162	-0.0851
5	A	0.0193	0.0202	**0.0319**	-0.137
6	A	0.0197	0.0215	**0.000559**	-0.235
7	A	0.0105	0.0109	**0.007399**	-0.174
7	B	0.00863	0.00894	**0.0167**	-0.240
8	A	0.0127	0.0127	0.0584	0.116
8	B	0.00828	0.00828	0.815	-0.0386

9	A	0.0121	0.0109	**0.00937**	0.165
9	B	0.0137	0.0136	0.815	0.0347
10	A	0.0125	0.0117	**0.00684**	0.187
11	B	0.0203	0.0209	0.894	-0.0121
12	B	0.0166	0.0174	0.815	-0.0641

Scenarios 3 and 4

Supplementary Figures 6 and 8 show the convergence of the objective function across 1000 generations during 100 independents ELA/GAopt runs for the ASD and CTL groups, respectively. To evaluate the consistency of selected ROIs, binomial tests were performed on the selection results from each group's 100 runs. Statistically significant ROIs after FDR correction are presented in Figure 6 and Supplementary Tables 6 (ASD) and 7 (CTL). The selection frequency distribution across all ROI candidates is shown in Supplementary Figures 7 (ASD) and 9 (CTL), reflecting how often each ROI was selected over 100 optimization trials.

Using the ASD-optimized ROIs from Cohort C, we estimated energy landscapes for both ASD and CTL groups. The number of local minima obtained for each group was computed, and a group comparison was performed using the Mann-Whitney U test. The test revealed that the ASD group exhibited a significantly lower number of local minima than the CTL group ($U_{200} = 4238.5,\ p = 0.043$, effect size r: 0.13), suggesting that the ASD-optimized ROI configuration captures group-specific features of brain state dynamics.

Conversely, using the CTL-optimized ROIs from Cohort D, the CTL group exhibited significantly fewer local minima than the ASD group ($U_{200} = 5924.5,\ p = 0.019$, effect size r: 0.16), again suggesting that the CTL-optimized ROIs capture group-specific differences in brain state dynamics.

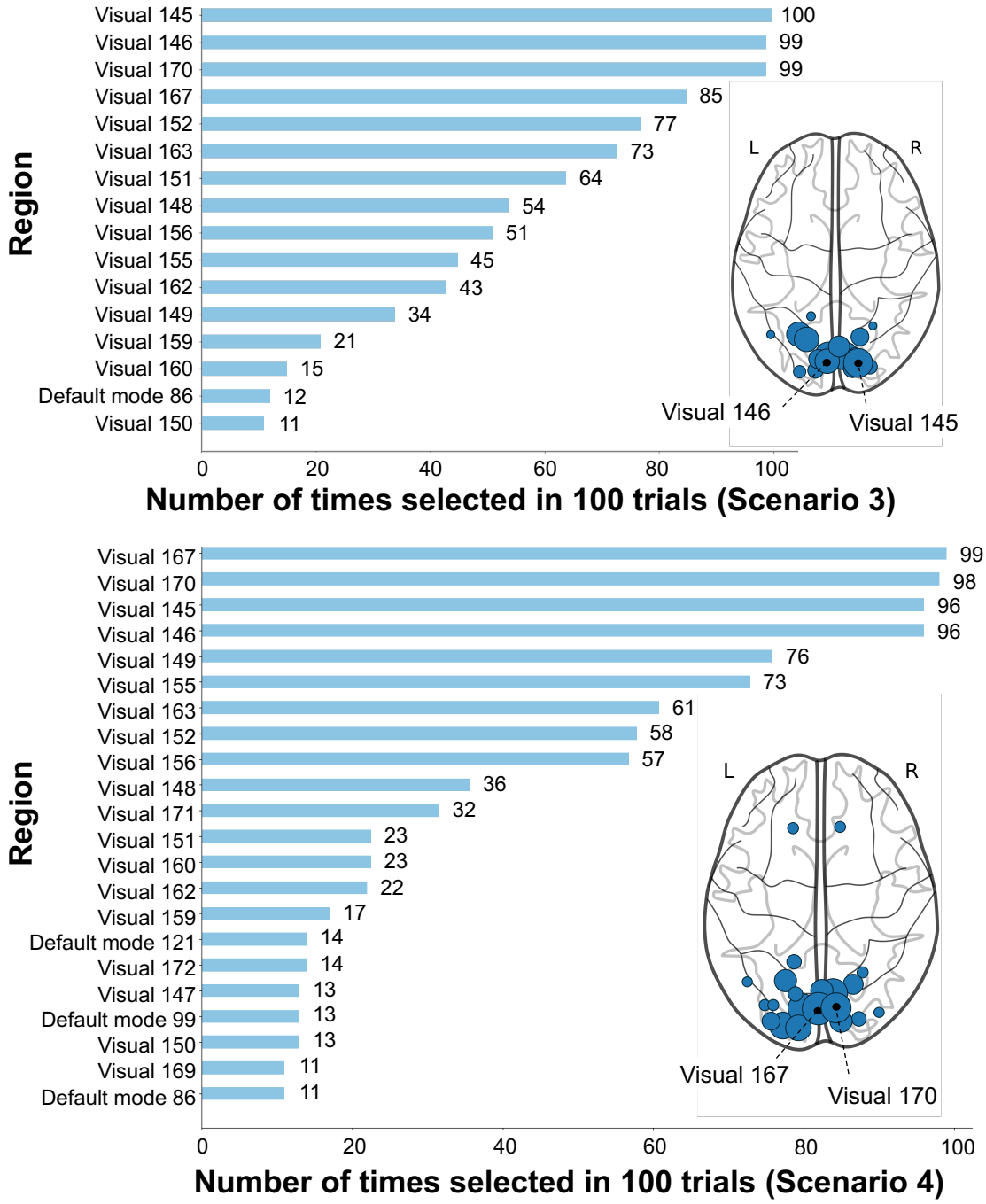

Figure 6 Selection frequency of each ROI across 100 runs of ELA/GAopt (Scenarios 3 and 4).

Discussion

Overview and advantages of the proposed method

The ELA/GAopt framework proposed in this study integrates energy landscape analysis with genetic algorithm-based feature selection, enabling objective, data-driven identification

of meaningful ROIs for the given dataset. By automating ROI selection based on pMEM fitting accuracy and inter-individual variability of the personalized inverse temperature parameter of pMEM, ELA/GAopt enhances reproducibility and objectivity in brain dynamics modeling.

Traditional ROI selection approaches in neuroimaging studies often depend on established anatomical or functional priorities derived from previous research. While such hypothesis-driven selection improves consistency across studies, it may also introduce confirmation bias, limiting the analysis framework to existing knowledge and potentially missing emergent patterns not captured by prior findings.

In contrast, ELA/GAopt mitigates this bias by enabling fully data-driven ROI selection. This allows the model to explore brain region combinations not considered a priori, thereby expanding the search space for novel insights into brain dynamics. Such exploratory capacity is particularly crucial for advancing our understanding of complex and heterogeneous conditions, such as ASD. Hereafter, we discuss the results obtained in multiple scenarios to demonstrate the effectiveness and clinical applicability of our proposed ELA/GAopt.

Evaluation of reproducibility (Scenario 1)

Scenario 1 evaluated the generalizability of ELA/GAopt using the publicly available Creativity dataset (OpenNeuro: ds002330), which includes resting-state fMRI data. ELA/GAopt was applied to the discovery set, and the optimized ROI sets were subsequently applied to the test set. These ROI sets achieved similarly high objective function values in both datasets (Figure 3B, C, E, and F; $p < 0.05$, FDR-corrected), demonstrating that ELA/GAopt avoids overfitting and yields generalizable ROI selection.

Moreover, the similarity of local minimum states between the discovery and test sets was significantly higher (Hamming distance difference was smaller) for ROI sets selected by ELA/GAopt than for randomly selected ROIs (Figure 3A and D; $p < 0.05$, FDR-corrected). Because local minimum represents stable brain states, this result suggests ELA/GAopt effectively identifies ROI sets capturing stable, reproducible patterns.

Reproducibility is a critical issue in neuroimaging research, especially for clinical translation. Traditional ROI-based analyses may underestimate reproducibility because fMRI signals are inherently non-stationary and exhibit considerable inter-individual and temporal variability.[40,41] In contrast, ELA/GAopt potentially enhances repeatability by excluding noisy or irrelevant features during ROI selection. Importantly, the objective

function of ELA/GAopt explicitly considers inter-individual variance (i.e., inverse temperature parameter of pMEM), which may further promote reproducibility in group-level energy landscape analyses. These improvements enhance the robustness of the findings and increase the potential for future clinical applications, including biomarker discovery and personalized modeling of brain dynamics.

Furthermore, the ROIs selected by ELA/GAopt were primarily centered in the occipital network. These regions play a central role in visual processing and are known to exhibit characteristic activity patterns even during the resting state.[42] Additionally, the angular gyrus, precuneus, and inferior temporal lobe, belonging to the default mode network (DMN), were also selected as ROIs. These areas are implicated in self-referential thought and memory integration, and are suggested to play a central role in resting-state brain activity.[43]

A noteworthy aspect of the ELA/GAopt-based ROI selection is that, compared to the default mode network, which has frequently been the focus of traditional resting-state brain activity studies, motor-related regions less frequently addressed and not mentioned in the original data sources were also selected.[29,44] These regions, which have been mainly studied concerning task-related activities, motor execution,[45] and postural control,[46] were found to potentially show important patterns of activity even in the resting state. Region selection aligns with prior research indicating that the dynamic coordination of multiple networks constitutes the human brain's resting-state activity.[44,47] This finding also encourages a reevaluation of the roles of new brain regions and network structures. The ELA/GAopt successfully identified these areas in a data-driven manner.

Detection of ASD-specific dynamics (Scenarios 2–4)

Scenarios 2, 3, and 4 employed the ABIDE II dataset to investigate whether ELA/GAopt could detect ASD-specific features in brain state dynamics.

In Scenario 2, ROIs selected by ELA/GAopt were mainly located within the sensory somatomotor hand network (Figure 4). Significant group differences in specific local minima probability were observed between the ASD and typically developing (CTL) groups (Table 1, Table 2 and Figure 5; $p < 0.05$, FDR-corrected). Notably, ASD participants more frequently visited local minimum characterized by the co-activation of all selected ROIs. This dynamic signature was replicated in an independent validation cohort (Cohort B), providing support for its robustness.

These findings are consistent with prior reports that identified local overconnectivity and long-range underconnectivity as characteristic features of brain organization in individuals with ASD.[48] The predominance of globally 'active' local minimum suggests excessive synchronization of neural activity in ASD, potentially reducing the flexibility of brain state transitions. This observation aligns with previous ELA studies showing overstability of neural dynamics,[13] and increased functional connectivity among visual and sensorimotor networks in infants with ASD, which correlated with symptom severity.[49] Moreover, manifold learning studies identified connectivity patterns in sensorimotor networks as discriminative features for distinguishing ASD from schizophrenia.[50]

Taken together, these results suggest that ASD is associated with a distinct neurodynamic profile characterized by reduced state variability and increased co-activation within specific functional networks. The ELA/GAopt demonstrated its effectiveness in uncovering such network-specific dynamic biomarkers in a fully data-driven manner.

Scenario 3 further evaluated this hypothesis by applying the ROI set optimized for the ASD group to the CTL group. The ROI sets optimized for the ASD group primarily consisted of visual network regions, as indicated in Figure 6. The application of the ASD-optimized ROIs to the ELA on the CTL group led to a significant increase in the number of observed local minima in CTL participants ($p < 0.05$), indicating that ASD-optimized ROIs poorly capture the neurodynamic patterns of typically developing individuals. This supports previous work suggesting that ASD is characterized by atypical over-coupling of visual networks, which may limit brain state transitions.[51,52]

Scenario 4 provided a complementary test by applying CTL-optimized ROIs to the ASD group. Similarly, the number of local minima observed in ASD participants was significantly increased ($p < 0.05$). Considering the results in Scenario 3, they suggest that the two groups exhibit fundamentally different brain state dynamics and network configurations. This further strengthens previous findings that ASD and CTL groups possess distinct neurodynamic architectures.[13,48–51,53]

These inter-application results suggest that ELA/GAopt can identify ROI sets that are not only discriminative but also specific to particular neurodevelopmental conditions. This highlights its potential utility for biomarker discovery and the study of condition-specific brain state dynamics.

With these results, our proposed ELA/GAopt demonstrates strong potential as a data-driven framework for identifying meaningful brain dynamics and holds promise for future applications in both basic and translational neuroscience research.

Data Availability

All the datasets used in this study are publicly available. The source codes of the proposed method are available on our GitHub repository (https://github.com/MIS-Lab-Doshisha/ela-gaopt).

Acknowledgements

We acknowledge the significant contributions of ABIDE-II and its primary source of funding: NIMH 5R21MH107045.

Funding

T.H. and S.H. were supported by JSPS KAKENHI Grant Number JP24K03028.

Competing Interests

The authors declare there are no competing interests.

References

1. Saberi M, Rieck JR, Golafshan S, et al. The brain selectively allocates energy to functional brain networks under cognitive control. *Sci Rep*. 2024;14:32032. doi:10.1038/s41598-024-83696-7
2. Watanabe T, Hirose S, Wada H, et al. A pairwise maximum entropy model accurately describes resting-state human brain networks. *Nat Commun*. 2013;4:1370. doi:10.1038/ncomms2388
3. Watanabe T, Hirose S, Wada H, et al. Energy landscapes of resting-state brain networks. *Front Neuroinformatics*. 2014;8. doi:10.3389/fninf.2014.00012
4. Ezaki T, Watanabe T, Ohzeki M, Masuda N. Energy landscape analysis of neuroimaging data. *Philos Trans R Soc Math Phys Eng Sci*. 2017;375(2096):20160287. doi:10.1098/rsta.2016.0287
5. Xing L, Guo Z, Long Z. Energy landscape analysis of brain network dynamics in

Alzheimer's disease. *Front Aging Neurosci*. 2024;16:1375091. doi:10.3389/fnagi.2024.1375091

6. Yamashita A, Rothlein D, Kucyi A, Valera EM, Esterman M. Brain state-based detection of attentional fluctuations and their modulation. *NeuroImage*. 2021;236:118072. doi:10.1016/j.neuroimage.2021.118072
7. Kondo HM, Terashima H, Ezaki T, Kochiyama T, Kihara K, Kawahara JI. Dynamic Transitions Between Brain States Predict Auditory Attentional Fluctuations. *Front Neurosci*. 2022;16:816735. doi:10.3389/fnins.2022.816735
8. Watanabe T, Masuda N, Megumi F, Kanai R, Rees G. Energy landscape and dynamics of brain activity during human bistable perception. *Nat Commun*. 2014;5:4765. doi:10.1038/ncomms5765
9. Kang J, Pae C, Park HJ. Graph-theoretical analysis for energy landscape reveals the organization of state transitions in the resting-state human cerebral cortex. *PLOS ONE*. 2019;14(9):e0222161. doi:10.1371/journal.pone.0222161
10. Kang J, Jeong SO, Pae C, Park HJ. Bayesian estimation of maximum entropy model for individualized energy landscape analysis of brain state dynamics. *Hum Brain Mapp*. 2021;42(11):3411-3428. doi:10.1002/hbm.25442
11. Jeong SO, Kang J, Pae C, et al. Empirical Bayes estimation of pairwise maximum entropy model for nonlinear brain state dynamics. *NeuroImage*. 2021;244:118618. doi:10.1016/j.neuroimage.2021.118618
12. Ezaki T, Sakaki M, Watanabe T, Masuda N. Age-related changes in the ease of dynamical transitions in human brain activity. *Hum Brain Mapp*. 2018;39(6):2673-2688. doi:10.1002/hbm.24033
13. Watanabe T, Rees G. Brain network dynamics in high-functioning individuals with autism. *Nat Commun*. 2017;8(1):16048. doi:10.1038/ncomms16048
14. Hosaka Y, Hieda T, Li R, Hayashi K, Jimura K, Matsui T. Surrogate data analyses of the energy landscape analysis of resting-state brain activity. *Front Neural Circuits*. 2025;19:1500227. doi:10.3389/fncir.2025.1500227
15. Masuda N, Islam S, Aung ST, Watanabe T. Energy landscape analysis based on the Ising model: Tutorial review. *PLOS Complex Syst*. 2025;2(5):e0000039. doi:10.1371/journal.pcsy.0000039
16. Tzourio-Mazoyer N, Landeau B, Papathanassiou D, et al. Automated anatomical labeling of activations in SPM using a macroscopic anatomical parcellation of the MNI MRI single-subject brain. *NeuroImage*. 2002;15(1):273-289. doi:10.1006/nimg.2001.0978
17. Power JD, Cohen AL, Nelson SM, et al. Functional network organization of the human

brain. *Neuron*. 2011;72(4):665-678. doi:10.1016/j.neuron.2011.09.006

18. Schaefer A, Kong R, Gordon EM, et al. Local-Global Parcellation of the Human Cerebral Cortex from Intrinsic Functional Connectivity MRI. *Cereb Cortex*. 2018;28(9):3095-3114. doi:10.1093/cercor/bhx179
19. Yeo BTT, Krienen FM, Sepulcre J, et al. The organization of the human cerebral cortex estimated by intrinsic functional connectivity. *J Neurophysiol*. 2011;106(3):1125-1165. doi:10.1152/jn.00338.2011
20. Hiwa S, Obuchi S, Hiroyasu T. Automated Extraction of Human Functional Brain Network Properties Associated with Working Memory Load through a Machine Learning-Based Feature Selection Algorithm. *Comput Intell Neurosci*. 2018;2018(1):4835676. doi:10.1155/2018/4835676
21. Szenkovits A, Meszlényi R, Buza K, Gaskó N, Lung RI, Suciu M. Feature Selection with a Genetic Algorithm for Classification of Brain Imaging Data. In: Stańczyk U, Zielosko B, Jain LC, eds. *Advances in Feature Selection for Data and Pattern Recognition*. Vol 138. Intelligent Systems Reference Library. Springer International Publishing; 2018:185-202. doi:10.1007/978-3-319-67588-6_10
22. Spedding AL, Di Fatta G, Cannataro M. A Genetic Algorithm for the selection of structural MRI features for classification of Mild Cognitive Impairment and Alzheimer's Disease. In: *2015 IEEE International Conference on Bioinformatics and Biomedicine (BIBM)*. IEEE; 2015:1566-1571. doi:10.1109/BIBM.2015.7359909
23. Wutzl B, Leibnitz K, Rattay F, Kronbichler M, Murata M, Golaszewski SM. Genetic algorithms for feature selection when classifying severe chronic disorders of consciousness. *PloS One*. 2019;14(7):e0219683. doi:10.1371/journal.pone.0219683
24. Oku M. okumakito/elapy. Published online May 30, 2025. Accessed July 7, 2025. https://github.com/okumakito/elapy
25. Ruffini G, Damiani G, Lozano-Soldevilla D, et al. LSD-induced increase of Ising temperature and algorithmic complexity of brain dynamics. *PLoS Comput Biol*. 2023;19(2):e1010811. doi:10.1371/journal.pcbi.1010811
26. Baeck T, Fogel DB, Michalewicz Z, eds. *Evolutionary Computation 1: Basic Algorithms and Operators*. CRC Press; 2018. doi:10.1201/9781482268713
27. Fortin FA, Rainville FMD, Gardner MA, Parizeau M, Gagné C. DEAP: Evolutionary Algorithms Made Easy. *J Mach Learn Res*. 2012;13(70):2171-2175.
28. Ishibuchi H, Kaige S, Narukawa K. Comparison Between Lamarckian and Baldwinian Repair on Multiobjective 0/1 Knapsack Problems. In: Coello Coello CA, Hernández Aguirre A, Zitzler E, eds. *Evolutionary Multi-Criterion Optimization*. Springer; 2005:370-385. doi:10.1007/978-3-540-31880-4_26

29. Sunavsky A, Poppenk J. Neuroimaging predictors of creativity in healthy adults. *NeuroImage*. 2020;206:116292. doi:10.1016/j.neuroimage.2019.116292
30. Di Martino A, Yan CG, Li Q, et al. The autism brain imaging data exchange: towards a large-scale evaluation of the intrinsic brain architecture in autism. *Mol Psychiatry*. 2014;19(6):659-667. doi:10.1038/mp.2013.78
31. Di Martino A, O'Connor D, Chen B, et al. Enhancing studies of the connectome in autism using the autism brain imaging data exchange II. *Sci Data*. 2017;4:170010. doi:10.1038/sdata.2017.10
32. thebrisklab/ABIDE_Preprocessing. Published online October 21, 2024. Accessed April 4, 2025. https://github.com/thebrisklab/ABIDE_Preprocessing
33. Nilearn. Nilearn. Accessed September 3, 2024. https://nilearn.github.io/index.html
34. Wang HT, Meisler SL, Sharmarke H, et al. Continuous Evaluation of Denoising Strategies in Resting-State fMRI Connectivity Using fMRIPrep and Nilearn. *BioRxiv Prepr Serv Biol*. Published online July 2023:2023.04.18.537240. doi:10.1101/2023.04.18.537240
35. Dosenbach NUF, Nardos B, Cohen AL, et al. Prediction of Individual Brain Maturity Using fMRI. *Science*. 2010;329(5997):1358-1361. doi:10.1126/science.1194144
36. Dosenbach NUF, Visscher KM, Palmer ED, et al. A Core System for the Implementation of Task Sets. *Neuron*. 2006;50(5):799-812. doi:10.1016/j.neuron.2006.04.031
37. Dosenbach NUF, Fair DA, Miezin FM, et al. Distinct brain networks for adaptive and stable task control in humans. *Proc Natl Acad Sci*. 2007;104(26):11073-11078. doi:10.1073/pnas.0704320104
38. Fair DA, Cohen AL, Power JD, et al. Functional Brain Networks Develop from a "Local to Distributed" Organization. *PLOS Comput Biol*. 2009;5(5):e1000381. doi:10.1371/journal.pcbi.1000381
39. Fox MD, Snyder AZ, Vincent JL, Corbetta M, Van Essen DC, Raichle ME. The human brain is intrinsically organized into dynamic, anticorrelated functional networks. *Proc Natl Acad Sci U S A*. 2005;102(27):9673-9678. doi:10.1073/pnas.0504136102
40. Song X, Panych LP, Chou YH, Chen NK. A Study of Long-Term fMRI Reproducibility Using Data-Driven Analysis Methods. *Int J Imaging Syst Technol*. 2014;24(4):339-349. doi:10.1002/ima.22111
41. Song X, Panych LP, Chen NK. Data-Driven and Predefined ROI-Based Quantification of Long-Term Resting-State fMRI Reproducibility. *Brain Connect*. 2016;6(2):136-151. doi:10.1089/brain.2015.0349
42. Zhang H, Tian J, Liu J, Li J, Lee K. Intrinsically organized network for face perception

during the resting state. *Neurosci Lett*. 2009;454(1):1-5. doi:10.1016/j.neulet.2009.02.054

43. Andrews-Hanna JR, Smallwood J, Spreng RN. The default network and self-generated thought: component processes, dynamic control, and clinical relevance. *Ann N Y Acad Sci*. 2014;1316(1):29-52. doi:10.1111/nyas.12360
44. Greicius MD, Krasnow B, Reiss AL, Menon V. Functional connectivity in the resting brain: a network analysis of the default mode hypothesis. *Proc Natl Acad Sci U S A*. 2003;100(1):253-258. doi:10.1073/pnas.0135058100
45. Sahin N, Mohan S, Maralani PJ, et al. Assignment Confidence in Localization of the Hand Motor Cortex: Comparison of Structural Imaging With Functional MRI. *Am J Roentgenol*. 2016;207(6):1263-1270. doi:10.2214/AJR.15.15119
46. Smith JA, Tain R, Sharp KG, et al. Identifying the neural correlates of anticipatory postural control: A novel fMRI paradigm. *Hum Brain Mapp*. 2023;44(10):4088-4100. doi:10.1002/hbm.26332
47. Seitzman BA, Snyder AZ, Leuthardt EC, Shimony JS. The State of Resting State Networks. *Top Magn Reson Imaging TMRI*. 2019;28(4):189-196. doi:10.1097/RMR.0000000000000214
48. Fu S, Wang X, Chen Z, et al. Abnormalities in brain complexity in children with autism spectrum disorder: a sleeping state functional MRI study. *BMC Psychiatry*. 2025;25:257. doi:10.1186/s12888-025-06689-4
49. Chen B, Linke A, Olson L, et al. Greater functional connectivity between sensory networks is related to symptom severity in toddlers with autism spectrum disorder. *J Child Psychol Psychiatry*. 2021;62(2):160-170. doi:10.1111/jcpp.13268
50. Hao X, Wang J, He Z, et al. Multi-Cluster Self-Paced Diverse Learning and Feature Fusion for Autism Spectrum Disorder Identification With Resting-State fMRI. *IEEE Trans Emerg Top Comput Intell*. 2024;8(6):3860-3873. doi:10.1109/TETCI.2024.3377551
51. Yamasaki T, Maekawa T, Fujita T, Tobimatsu S. Connectopathy in Autism Spectrum Disorders: A Review of Evidence from Visual Evoked Potentials and Diffusion Magnetic Resonance Imaging. *Front Neurosci*. 2017;11:627. doi:10.3389/fnins.2017.00627
52. Sadeghian F, Hasani H, Jafari M. Feature Selection Based on Genetic Algorithm in the Diagnosis of Autism Disorder by fMRI. *Casp J Neurol Sci*. 2021;7(2):74-83. doi:10.32598/CJNS.7.25.5
53. Kozhemiako N, Nunes AS, Vakorin V, Iarocci G, Ribary U, Doesburg SM. Alterations in Local Connectivity and Their Developmental Trajectories in Autism Spectrum

Disorder: Does Being Female Matter? *Cereb Cortex N Y N 1991*. 2020;30(9):5166-5179. doi:10.1093/cercor/bhaa109

Figure legends

Figure 1 Schematic overview of ELA/GAopt framework.

The proposed framework ELA/GAopt combines energy landscape analysis (ELA) with a genetic algorithm (GA)-based optimization for automatic region of interest (ROI) selection. (**A**) Candidate ROI sets are generated as binary vectors by the GA, where each gene indicates whether a specific ROI is selected (1) or not (0). (**B**) Brain activity data are extracted from the selected ROIs. (**C**) The brain activity data are binarized (active: 1 or inactive: -1) to form discrete activation patterns over time. (**D**) The frequency of occurrence of each available activation pattern is analyzed. (**E**) A pairwise maximum entropy model (pMEM) is fitted to the binarized time series data to estimate the energy associated with each observed signal pattern. The resulting energy landscape visualizes the probability and energy of each activation pattern, characterizing brain dynamics. (**F**) A two-step pMEM parameter optimization method, in which the inverse temperature parameter—which defines the Boltzmann distribution—is optimized for each individual dataset while keeping the group-derived pMEM parameters fixed. (**G**) The ELA-derived parameters (e.g., model accuracy and personalized parameters) are fed back into the GA as a fitness score to evaluate each candidate ROI set. The GA then iteratively updates the ROI sets through selection, crossover, mutation, and repair operations.

Figure 2 Selection frequency of each ROI across 100 runs of ELA/GAopt (Scenario 1).

The bar graph illustrates the frequency with which each ROI was selected across 100 independent optimization runs. A binomial test was used to determine if the frequency of each ROI was higher than chance, and 18 ROIs were found to be statistically significant ($p < 0.05$, FDR-corrected) and indicated in the figure. The ROIs are arranged in order from most to least frequently selected. Their anatomical locations are also displayed on the glass brain plot. The circle size in the brain plot represents the frequency at which each ROI was chosen, with larger circles indicating higher frequencies.

Figure 3 Reproducibility of local minimum patterns across discovery and test datasets.

(A - C) Visualization of the distributions of the difference in means between optimized ROIs and randomly selected ROIs generated from 10,000 permutations. The solid dashed line indicates the observed difference in means. (D - F) The horizontal bar within the colored

area indicates the median, and the top and bottom of the colored area represent the 75th and 25th percentiles, respectively. Whiskers extend to the minimum and maximum values within 1.5 times the interquartile range. Asterisks denote statistical significance ($*$:$p < 0.05$). (D) The Hamming distances between ID vectors of the discovery ($n = 31$) and test ($n = 30$) datasets. The Hamming distances were significantly smaller for the optimized ROIs compared to the randomly selected ROIs (permutation test, $p = 0.0025$, FDR-corrected, Cohen's $d = 0.408$). (E) The objective function values in the discovery data for the optimized ROI sets were significantly higher than those of the randomly selected sets (permutation test, $p < 0.001$, FDR-corrected, Cohen's $d = 5.63$). (F) The significant advantage of optimized ROI sets also generalized to the test set when compared to randomly selected sets (permutation test, $p < 0.001$, FDR-corrected, Cohen's $d = 2.51$). The dataset included optimized ROIs ($n = 100$), randomly selected ROIs ($n = 100$).

Figure 4 Selection frequency of each ROI across 100 runs of ELA/GAopt (Scenario 2).

The bar graph illustrates the frequency with which each ROI was selected in 100 independent optimization runs. A binomial test was used to determine if the selection frequency of each ROI was higher than chance, and 14 ROIs were found to be statistically significant ($p < 0.05$, FDR-corrected), as shown in the figure. The ROIs are arranged in order from most to least frequently selected. Their anatomical locations are also displayed on the glass brain plot. The circle size in the brain plot represents the frequency of each ROI's selection, with larger circles indicating higher frequencies.

Figure 5 Observed local minimum states for representative trials 1 (A) and 2 (B).

State numbers are assigned to indicate unique binary activity patterns.

Figure 6 Selection frequency of each ROI across 100 runs of ELA/GAopt (Scenarios 3 and 4).

The bar graph illustrates the frequency with which each ROI was selected across 100 independent optimization runs. A binomial test was performed to determine whether the frequency of each ROI exceeded chance levels. As a result, 16 ROIs were identified as statistically significant in Scenario 3 and 22 ROIs in Scenario 4 ($p < 0.05$, FDR-corrected). The ROIs are sorted in descending order of selection frequency. Their anatomical locations are also displayed on the glass brain plot. The circle size in the brain plot represents the frequency of each ROI's selection, with larger circles indicating higher frequencies.

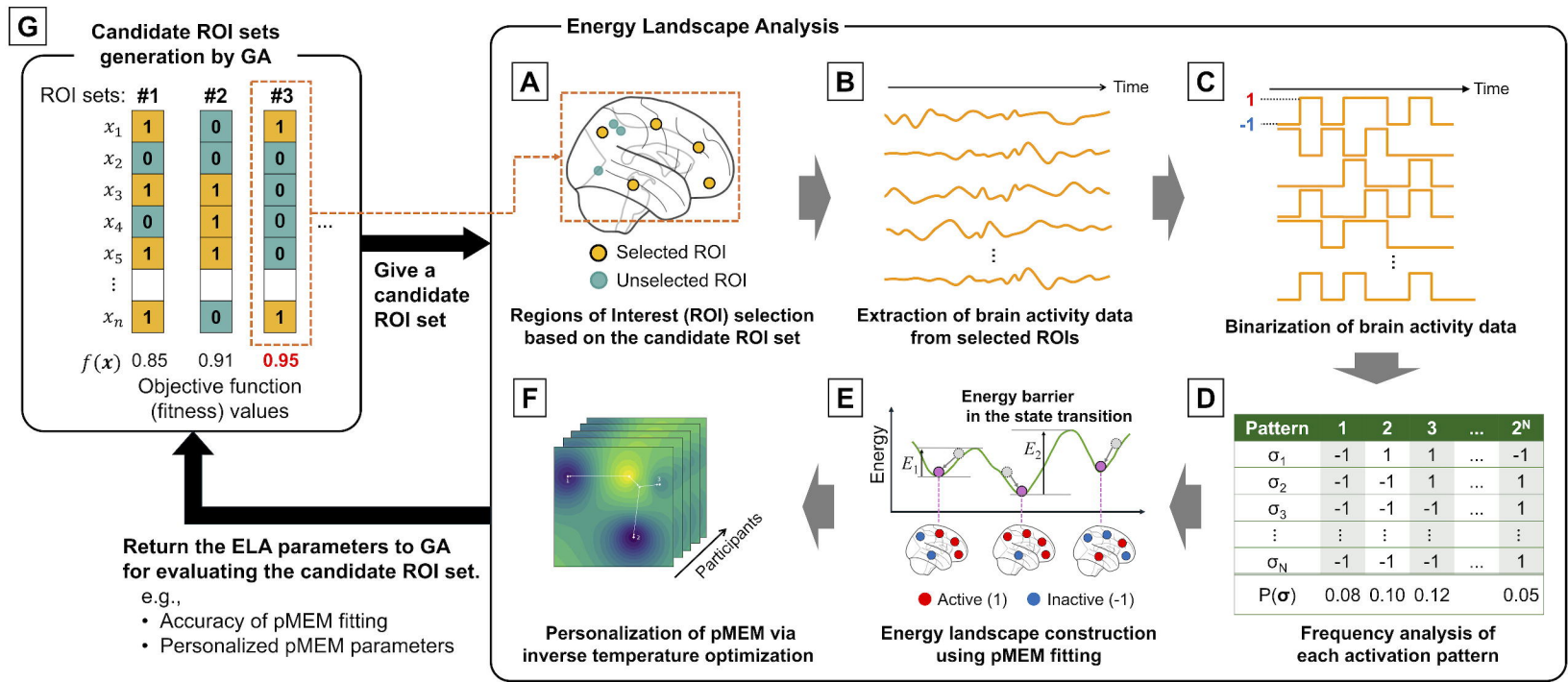
G
Candidate ROI sets generation by GA
ROI sets: #1 #2 #3
x_1 1 0 1
x_2 0 0 0
x_3 1 1 0
x_4 0 1 0
x_5 1 1 0
x_n 1 0 1
$f(x)$ 0.85 0.91 0.95
Objective function (fitness) values
Give a candidate ROI set
Return the ELA parameters to GA for evaluating the candidate ROI set.
e.g.,
• Accuracy of pMEM fitting
• Personalized pMEM parameters
Energy Landscape Analysis
A
Selected ROI
Unselected ROI
Regions of Interest (ROI) selection based on the candidate ROI set
B
Time
Extraction of brain activity data from selected ROIs
C
Time
1
-1
Binarization of brain activity data
D
Pattern 1 2 3 ... 2^N
σ_1 -1 1 1 ... -1
σ_2 -1 -1 1 ... 1
σ_3 -1 -1 -1 ... 1
σ_N -1 -1 -1 ... 1
P(σ) 0.08 0.10 0.12 0.05
Frequency analysis of each activation pattern
E
Energy barrier in the state transition
Energy
E_1
E_2
Active (1)
Inactive (-1)
Energy landscape construction using pMEM fitting
F
Participants
Personalization of pMEM via inverse temperature optimization

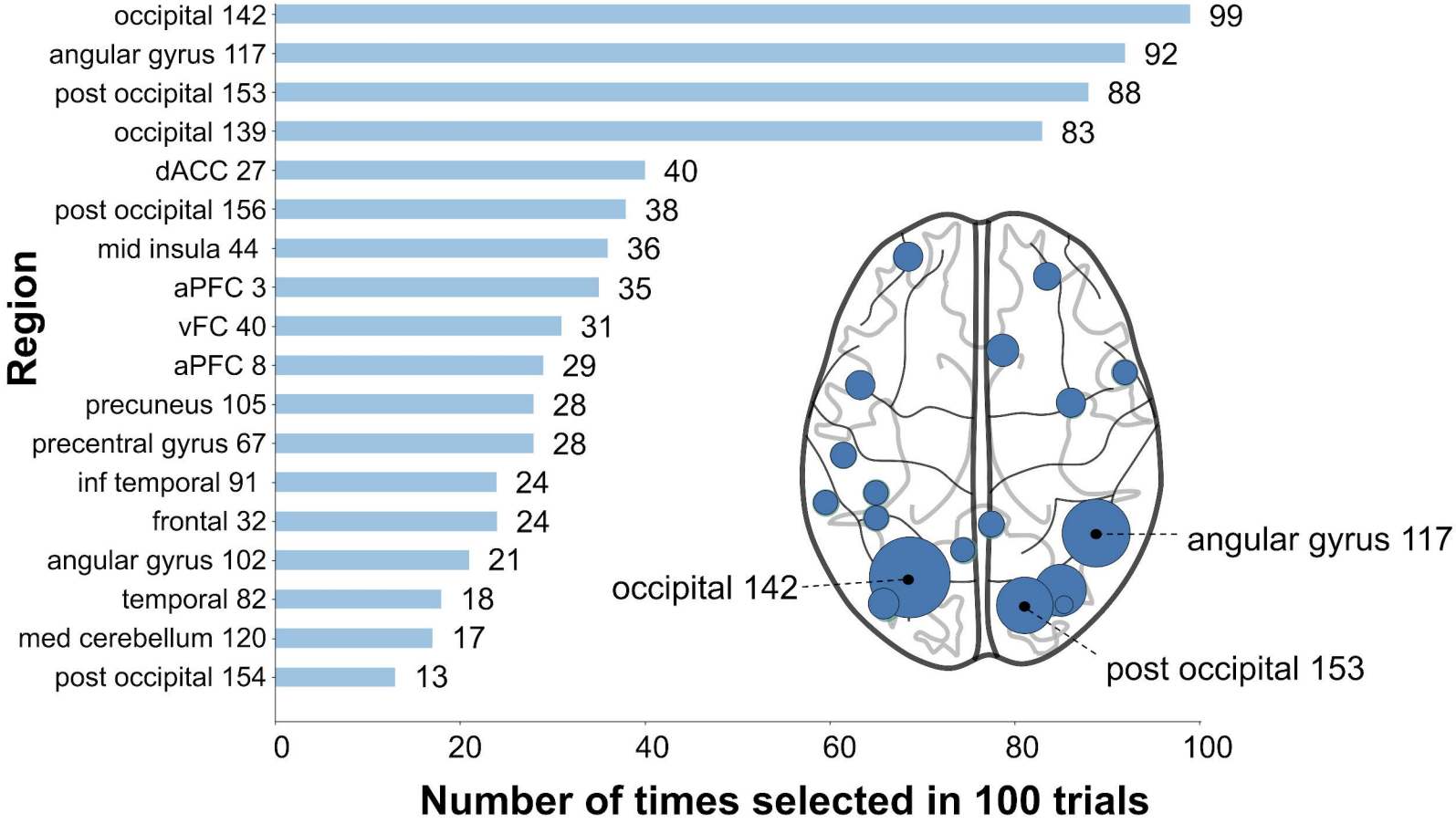
occipital 142
angular gyrus 117
post occipital 153
occipital 139
dACC 27
post occipital 156
mid insula 44
aPFC 3
vFC 40
aPFC 8
precuneus 105
precentral gyrus 67
inf temporal 91
frontal 32
angular gyrus 102
temporal 82
med cerebellum 120
post occipital 154
99
92
88
83
40
38
36
35
31
29
28
28
24
24
21
18
17
13
Region
0
20
40
60
80
100
Number of times selected in 100 trials
angular gyrus 117
occipital 142
post occipital 153

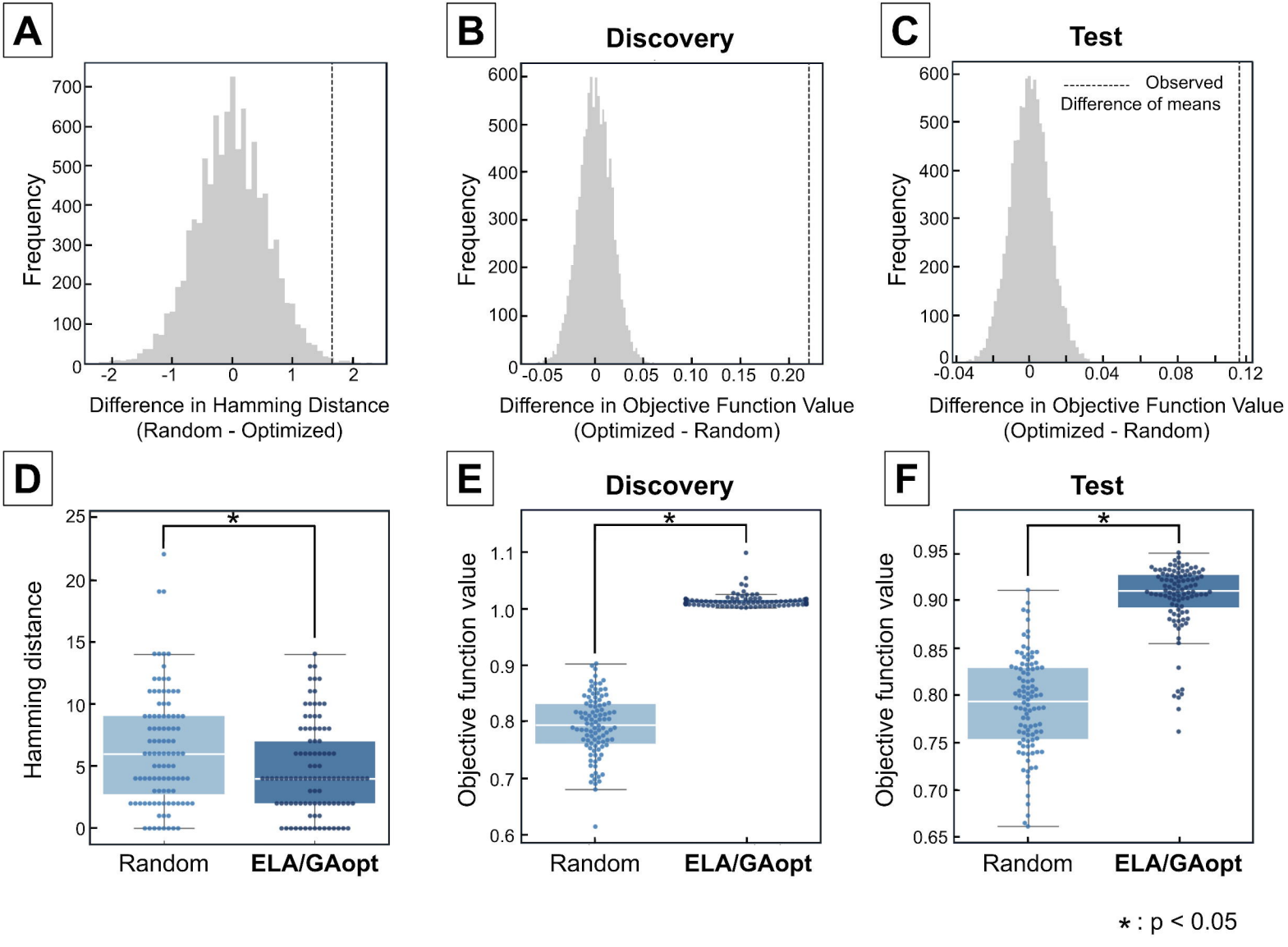
A
Frequency
Difference in Hamming Distance
(Random - Optimized)
B
Discovery
Frequency
Difference in Objective Function Value
(Optimized - Random)
C
Test
Observed
Difference of means
Frequency
Difference in Objective Function Value
(Optimized - Random)
D
Hamming distance
Random
ELA/GAopt
E
Discovery
Objective function value
Random
ELA/GAopt
F
Test
Objective function value
Random
ELA/GAopt
* : p < 0.05

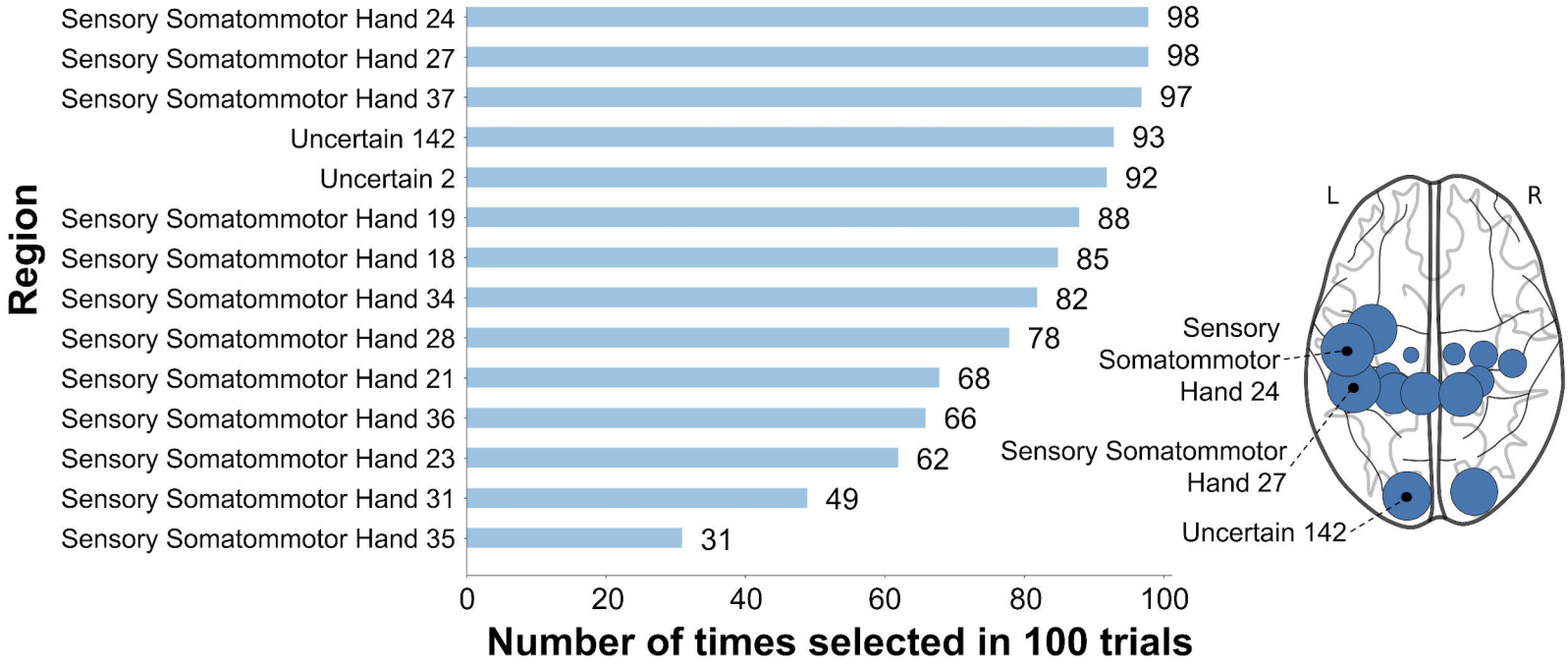
Region
Sensory Somatommotor Hand 24
Sensory Somatommotor Hand 27
Sensory Somatommotor Hand 37
Uncertain 142
Uncertain 2
Sensory Somatommotor Hand 19
Sensory Somatommotor Hand 18
Sensory Somatommotor Hand 34
Sensory Somatommotor Hand 28
Sensory Somatommotor Hand 21
Sensory Somatommotor Hand 36
Sensory Somatommotor Hand 23
Sensory Somatommotor Hand 31
Sensory Somatommotor Hand 35
98
98
97
93
92
88
85
82
78
68
66
62
49
31
0
20
40
60
80
100
Number of times selected in 100 trials
L
R
Sensory Somatommotor Hand 24
Sensory Somatommotor Hand 27
Uncertain 142

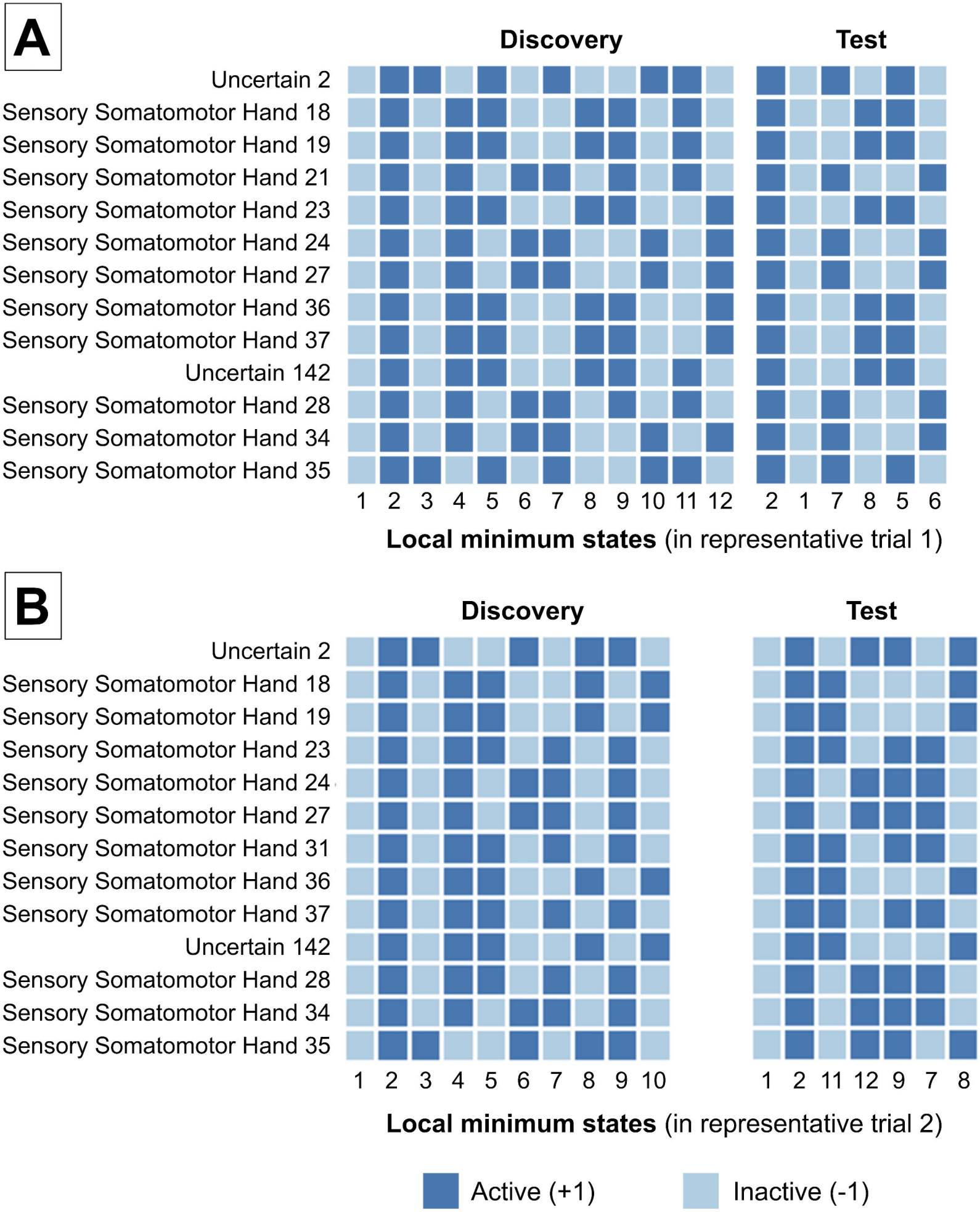
A
Discovery
Test
Uncertain 2
Sensory Somatomotor Hand 18
Sensory Somatomotor Hand 19
Sensory Somatomotor Hand 21
Sensory Somatomotor Hand 23
Sensory Somatomotor Hand 24
Sensory Somatomotor Hand 27
Sensory Somatomotor Hand 36
Sensory Somatomotor Hand 37
Uncertain 142
Sensory Somatomotor Hand 28
Sensory Somatomotor Hand 34
Sensory Somatomotor Hand 35
1 2 3 4 5 6 7 8 9 10 11 12
2 1 7 8 5 6
Local minimum states (in representative trial 1)
B
Discovery
Test
Uncertain 2
Sensory Somatomotor Hand 18
Sensory Somatomotor Hand 19
Sensory Somatomotor Hand 23
Sensory Somatomotor Hand 24
Sensory Somatomotor Hand 27
Sensory Somatomotor Hand 31
Sensory Somatomotor Hand 36
Sensory Somatomotor Hand 37
Uncertain 142
Sensory Somatomotor Hand 28
Sensory Somatomotor Hand 34
Sensory Somatomotor Hand 35
1 2 3 4 5 6 7 8 9 10
1 2 11 12 9 7 8
Local minimum states (in representative trial 2)
Active (+1)
Inactive (-1)

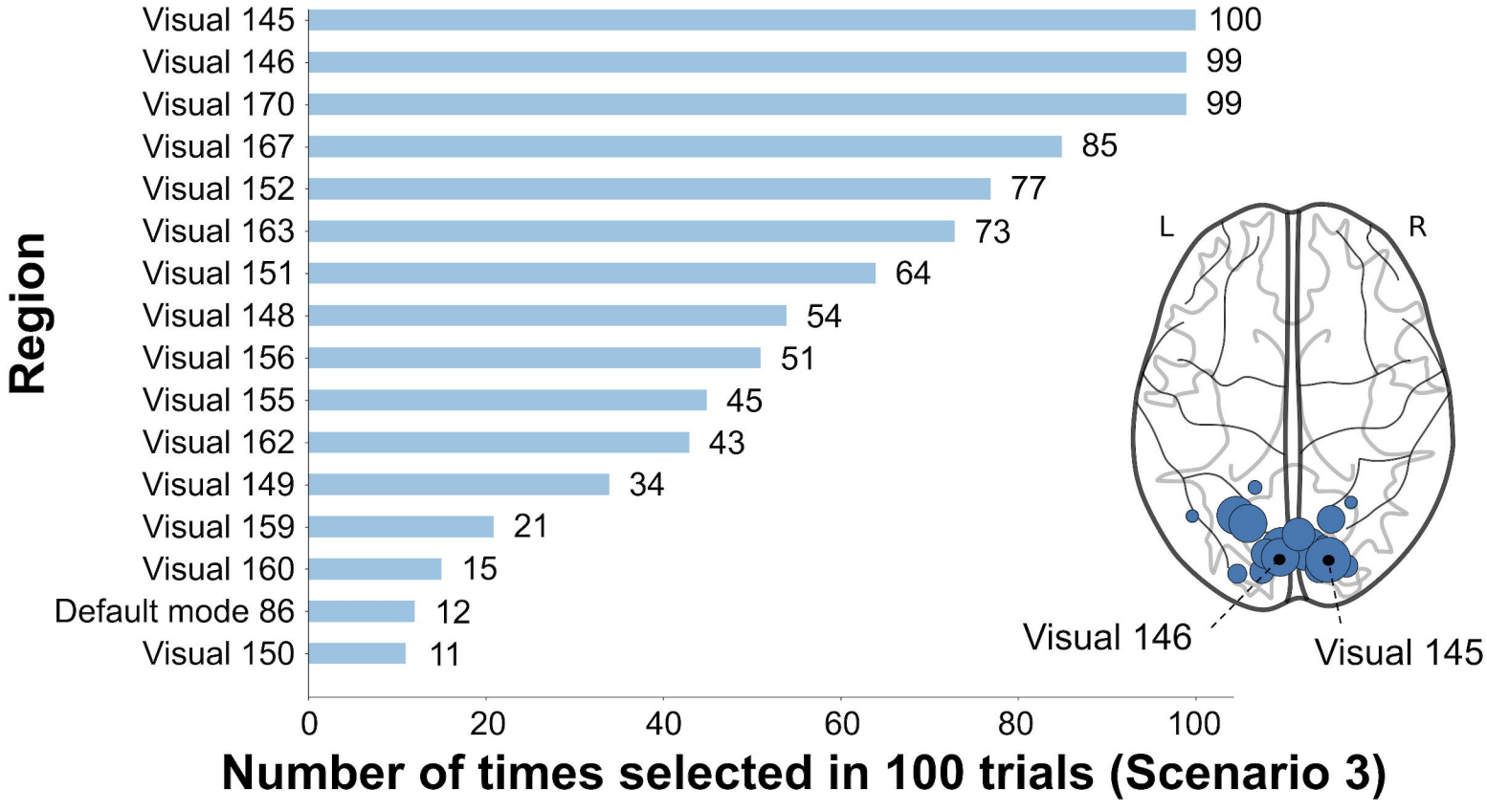
Region
Visual 145 100
Visual 146 99
Visual 170 99
Visual 167 85
Visual 152 77
Visual 163 73
Visual 151 64
Visual 148 54
Visual 156 51
Visual 155 45
Visual 162 43
Visual 149 34
Visual 159 21
Visual 160 15
Default mode 86 12
Visual 150 11
0 20 40 60 80 100
Number of times selected in 100 trials (Scenario 3)
L
R
Visual 146
Visual 145

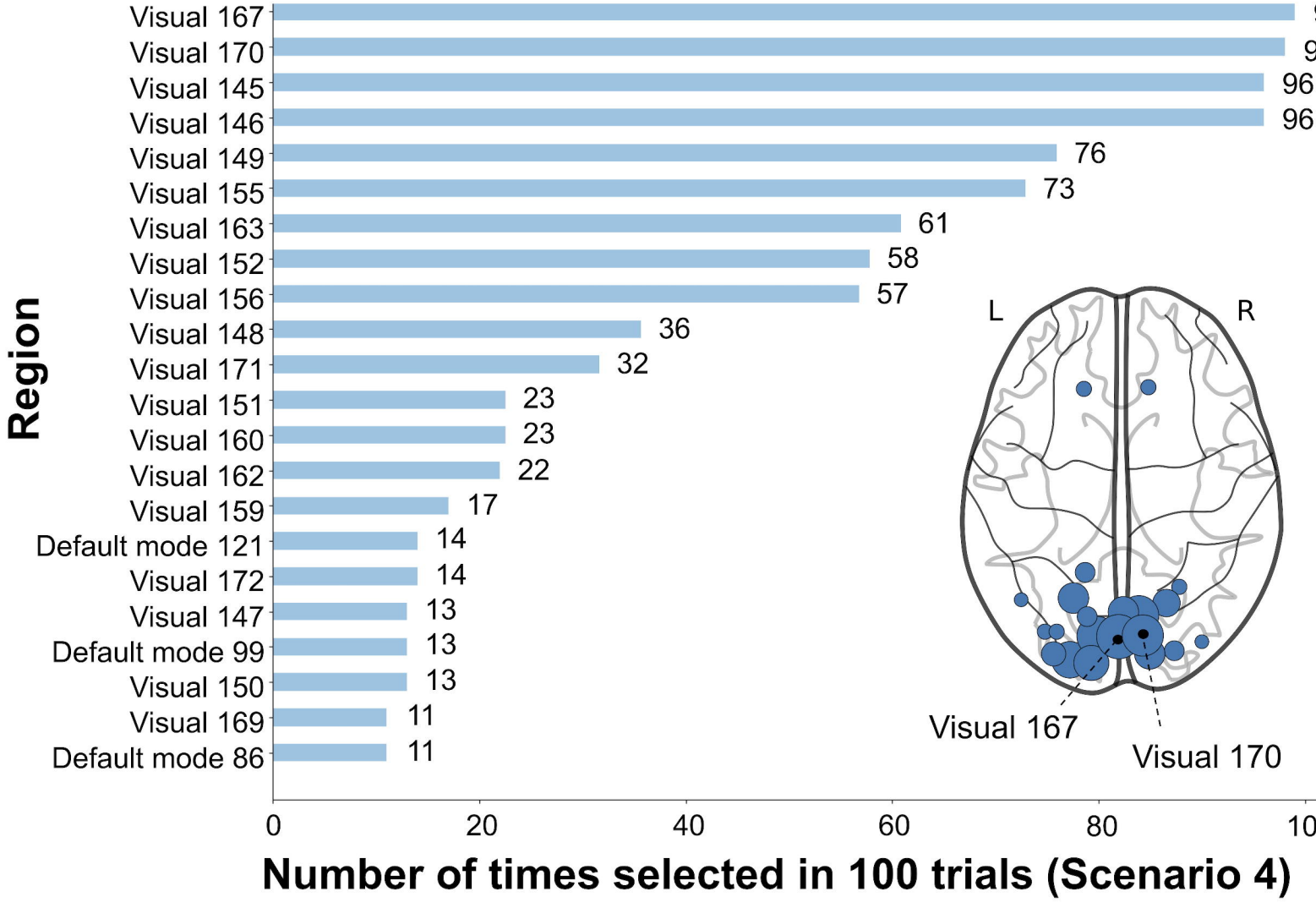
Region
Visual 167 99
Visual 170 98
Visual 145 96
Visual 146 96
Visual 149 76
Visual 155 73
Visual 163 61
Visual 152 58
Visual 156 57
Visual 148 36
Visual 171 32
Visual 151 23
Visual 160 23
Visual 162 22
Visual 159 17
Default mode 121 14
Visual 172 14
Visual 147 13
Default mode 99 13
Visual 150 13
Visual 169 11
Default mode 86 11
0 20 40 60 80 100
Number of times selected in 100 trials (Scenario 4)
L
R
Visual 167
Visual 170